

# The Structures of Distant Galaxies V: The Evolution of Galaxy Structure in Stellar Mass at $z < 1$

M. M. Lanyon-Foster<sup>1</sup>, C. J. Conselice<sup>1\*</sup>, M. R. Merrifield<sup>1</sup>

<sup>1</sup>*University of Nottingham, School of Physics & Astronomy, Nottingham, NG7 2RD UK*

Accepted ; Received ; in original form

## ABSTRACT

Galaxy structure and morphology is nearly always studied using the light originating from stars, however ideally one is interested in measuring structure using the stellar mass distribution. Not only does stellar mass trace out the underlying distribution of matter it also minimises the effects of star formation and dust on the appearance and structure of a galaxy. We present in this paper a study of the stellar mass distributions and structures of galaxies at  $z < 1$  as found within the GOODS fields. We use pixel by pixel K-corrections to construct stellar mass and mass-to-light ratio maps of 560 galaxies of known morphology at magnitudes  $z_{850} < 24$ . We measure structural and size parameters using these stellar mass maps, as well as on ACS *BViz* band imaging. This includes investigating the structural *CAS*–Gini– $M_{20}$  parameters and half-light radius ( $R_e$ ) for each galaxy. We further identify and examine unusual galaxy types with this method, including compact and peculiar ellipticals, and peculiar galaxies in some mode of formation. We compare structural parameters and half-light radii in the ACS  $z_{850}$ -band and stellar mass maps, finding no systematic bias introduced by measuring galaxy sizes in  $z_{850}$ . We furthermore investigate relations between structural parameters in the ACS *BViz* bands and stellar mass maps, and compare our result to previous morphological studies. Combinations of various parameters in stellar mass generally reveal clear separations between early and late type morphologies, but cannot easily distinguish between star formation and dynamically disturbed systems. We also show that while ellipticals and early-type spirals have fairly constant *CAS* values at  $z < 1$  we find a tendency for late-type spiral and peculiar morphological types to have a higher  $A(M_*)$  at higher redshift. We argue that this, and the large fraction of peculiars that appear spiral-like in stellar mass maps, are possible evidence for either an active bulge formation in some late-type disks at  $z < 1$  or the presence of minor merger events.

**Key words:** Galaxies: Structure, Morphology, Classification, Evolution

## 1 INTRODUCTION

One of the most intriguing questions in modern astronomy is how the universe assembled into the structures we see today. A major part of this question is understanding how galaxies formed over cosmic time. A popular and rapidly developing method of tracing the evolution of galaxies is through examining galaxy morphologies and structures over a range of redshifts (e.g. Conselice 2003; Conselice, Rajgor & Myers 2008; Conselice et al. 2009; Lotz et al. 2008; Cassata et al. 2010; Ricciardelli et al. 2010; Weinzirl et al. 2011). While understanding how the morphologies of galaxies evolve, and how matter in galaxies is structured, is fundamental, struc-

tural studies of galaxies have thus far focused on measuring properties in one or more photometric bands, and using this as a tracer of evolution. These types of structural analyses have always been measured in terms of relative luminosities, such that brighter parts of galaxies contribute more towards their structure and morphology. To understand galaxies more fully however, it is important to study the evolution of galaxy structure in terms of their stellar mass distribution, as this better reflects the underlying distribution of stars in a galaxy.

Morphological studies have evolved from initial attempts to describe the range of galaxy forms during the early-mid 20th century, towards modern efforts of linking the spatial distribution of a galaxy’s stars to its formation history. In the move away from visual classifications, the

\* E-mail: conselice@nottingham.ac.uk

goal has been to quantify galaxy structure/morphology in a way such that structures can be measured automatically and in a reliable way. There are two broad approaches for automated classification of galaxies - the parametric and non-parametric methods.

In the parametric approach, the light profiles of galaxies, as seen in the plane of the sky, are compared with predetermined analytic functions. For example, single Sersic profiles are fit to an entire galaxy’s light profile. Similarly, bulge-to-disc ( $B/D$ ) light ratios are computed by fitting two component profiles to a galaxy. These methods are however unable to parameterise directly any star formation or merging activity which produces random or asymmetric structures within galaxies. The “non-parametric” structural approaches have no such presumed light profiles implicit in their analyses (e.g., Shade et al. 1995; Abraham et al. 1996; Conselice 1997, 2003; Lotz et al. 2004). This is a more natural approach towards measuring galaxy structures, as the majority of galaxies in the distant Universe have irregular structures that are not well fit by parameterised forms (e.g. Conselice et al. 2005; Conselice, Rajgor & Myers 2008). Perhaps the most successful and straightforward of the non-parametric systems is the *CAS* method, which uses a combination of concentration ( $C$ ), asymmetry ( $A$ ) and clumpiness ( $S$ ) values to separate galaxy types (Conselice et al. 2000; Bershadsky et al. 2000; Conselice 2003).

Besides overall structure, the measurement of the size evolution of galaxies, as measured through half-light radii, also has important implications for their formation histories. For example, many studies such as Trujillo et al. (2007) and Buitrago et al. (2008) have measured galaxy sizes for systems at  $z > 1$  and have found a population of compact spheroid galaxies with number densities two orders of magnitude higher than what we find in the local universe. The absence of a significant number of these small sized (as measured by half-light radii), high mass galaxies in the local Universe suggests that this population has evolved and has perhaps merged with other galaxies. However, these studies are measured based on the light originating from these galaxies, and it is not clear whether sizes would change when measured using the distribution of stellar mass rather than light.

All of these methods for measuring the resolved structures of high redshift galaxies depend on measurements made in one or more photometric bands. As such, quantitative structures are influenced by a combination of effects, including: regions of enhanced star formation, irregular dust distributions, differing ages and metallicities of stellar populations and minor/major mergers. The morphology and structure of a galaxy also depends strongly upon the rest-frame wavelength probed (e.g., Windhorst et al. 2002; Taylor-Mager et al. 2007). Young stars, such as OB stars can dominate the appearances of galaxies at blue wavelengths, thereby giving a biased view of the underlying mass within the galaxy. Longer wavelength observations improve the situation, but at every wavelength, the light emitted is from a mixture of stars at a variety of ages and the dust content. More fundamental is the structure of the stellar mass distribution with a galaxy, as it is more of a direct tracer of the underlying potential. Although galaxy structure has been measured on rest-frame near-infrared and  $I$ -band imaging,

which traces stellar mass to first order, we directly investigate the stellar mass images within this paper.

We use the method outlined in Lanyon-Foster, Conselice & Merrifield (2007; LCM07) to reconstruct stellar mass maps of galaxies within the GOODS fields at  $z < 1$ . We then use this to investigate the evolution of the distribution of galaxy stellar mass during the last half of the universe’s history. We use these stellar mass maps to directly measure *CAS* parameters, and the sizes of these galaxies in stellar mass over this epoch. We test the assumptions that the *CAS* parameters and sizes can be reliably measured in optical light by comparing the parameters for these galaxies measured in the  $B_{435}$ ,  $V_{606}$ ,  $i_{775}$ , and  $z_{850}$  bands and in stellar mass. We finally investigate how these various wavelengths and stellar mass maps can be used to classify galaxies by their formation modes, revealing how these systems are assembling.

This paper is organised as follows: in § 2 and § 3 we describe the data, sample selection and method, including explanations of the K-correction code we use and the *CAS* analysis. In § 4 we present our results, discussing the stellar mass maps themselves, the comparison between galaxy size and the *CAS* parameters in  $z_{850}$  and mass. We then explore the relations between the structural parameters in  $B_{435}$ ,  $V_{606}$ ,  $i_{775}$ ,  $z_{850}$  and stellar mass. Finally, in § 5, we discuss our conclusions and comment on future applications. Throughout we assume a standard cosmology of  $H_0 = 70$  km s<sup>-1</sup> Mpc<sup>-1</sup>, and  $\Omega_m = 1 - \Omega_\Lambda = 0.3$ .

## 2 DATA AND SAMPLE

### 2.1 Data

The primary source of our data consists of HST/ACS imaging from the GOODS ACS imaging Treasury Program<sup>1</sup>. The observations consist of imaging in the  $B_{435}$  (F435W),  $V_{606}$  (F606W),  $i_{775}$  (F775W) and  $z_{850}$  (F850LP) pass-bands, covering the Hubble Deep Field-North (HDF-N) area. The central wavelengths of these filters, and their full-width at half-maximum, are: F435W (4297, 1038 Å), F606W (5907, 2342 Å), F775W (7764, 1528 Å), F850L (9445, 1229 Å). The images have been reduced (using the ACS CALACS pipeline), calibrated, stacked and mosaiced by the GOODS team (Giavalisco et al. 2004). The field is provided in many individual image sections, with the HDF-N data divided into 17 sections, each of  $8192 \times 8192$  pixels. The total area of the GOODS survey is roughly 315 arcmin<sup>2</sup>, and we utilise imaging which was drizzled with a pixel scale of 0.03 arcsec pixel<sup>-1</sup>, giving an effective PSF size of  $\sim 0.1''$  in the  $z$ -band.

The sample consists of galaxies selected in the GOODS-N field with  $z \leq 1$  and a F814W magnitude of  $< 24$ . The sample was also restricted to those galaxies with data in all four ACS photometric bands such that we can subsequently obtain the most accurate K-corrections and stellar masses possible. The final sample consists of 560 objects, which were individually cut out of the GOODS-N ACS imaging, and handled as separate entities. This is described in detail in the following section.

<sup>1</sup> <http://archive.stsci.edu/prepds/goods/>

Photometric redshifts are available for the whole sample (Mobasher et al. 2004), and spectroscopic redshifts are available for 404 out of 560 galaxies, as found by the Team Keck Redshift Survey (TKRS; Wirth et al., 2004). When spectroscopic redshifts are available they are used, else the photometric values are substituted.

### 3 METHOD

#### 3.1 Stellar Mass Maps

To create stellar mass maps of our galaxies, each pixel in each galaxy image is treated individually throughout the analysis. We convert fluxes from counts per pixel to apparent magnitudes per square arc-second for each pixel in every image in all four photometric bands, as well as calculating their associated errors. Pixels with negative fluxes were assigned values four orders of magnitude smaller than the typical flux so that even pixels with low signal-to-noise values can be mapped. This however means that our resulting values for the CAS parameters, especially asymmetry which uses the background light to do a correction, are potentially different than when measured using optical light.

Because our galaxies are at a variety of redshifts, we have to carry out fitting to each SED for each pixel to calculate the stellar mass within each pixel. K-corrections and stellar masses are calculated for each pixel of each image using the ‘‘K-Correct’’ code of Blanton & Roweis (2007). This is similar to previous methods outlined by Lanyon-Foster et al. (2007), Bothun (1986), Abraham et al. (1999), and Welikala et al. (2008, 2011).

The code, K-Correct<sup>2</sup> naturally handles large datasets, and through its interpretation of the data in terms of physical stellar population models, outputs results in terms of stellar mass and star formation histories (SFHs) of each galaxy. The code allows the input of GOODS data and outputs a stellar mass for each object. The code can also be modified so as to treat each pixel as a separate input object, which we do in this work.

The K-correction ( $K_{QR}(z)$ ) between bandpass  $R$ , used to observe a galaxy with apparent magnitude ( $m_R$ ), at redshift  $z$ , and the desired bandpass  $Q$  is defined as (e.g., Oke & Sandage 1968):

$$m_R = M_Q + DM(z) + K_{QR}(z) - 5\log(h) \quad (1)$$

where

$$DM(z) = 25 + 5\log\left[\frac{d_L}{h^{-1}\text{Mpc}}\right] \quad (2)$$

is the bolometric distance modulus calculated from the luminosity distance,  $d_L$ ,  $M_Q$  is the absolute magnitude and  $h = H_0/100 \text{ km s}^{-1} \text{ Mpc}^{-1}$ .

The K-correct software contains model templates in electronic form and an implementation of the method to fit data to models. The code uses the stellar population synthesis models of Bruzual & Charlot (2003) and contains training sets of data from GALEX, SDSS, 2MASS, DEEP2 and GOODS. The code finds the nonnegative linear combination of  $N$  template star formation histories that best match the

observations using a minimum  $\chi^2$  comparison. With the entire set of galaxy observations available, K-correct also fits for the  $N$  template SFHs using a nonnegative matrix factorisation algorithm. K-correct naturally handles data uncertainties, missing data, and deals with the complications of observing galaxy spectra photometrically, using broad-band filters of galaxies at varying redshifts.

We use a set of 485 spectral templates to fit to our galaxy pixel SEDs using Bruzual & Charlot (2003) models with the Chabrier (2003) IMF and Padova (1994) isochrones. All of the six metallicities available (mass fractions of elements heavier than He of  $Z = 0.0001, 0.0004, 0.004, 0.008, 0.02$  and  $0.05$ ) are used.

Some of the known areas of uncertainty in the stellar population models are in the UV and IR regions. In the UV light from young or intermediate aged stellar populations can dominate the flux at  $\sim 1500\text{\AA}$ . In the near-IR, thermally pulsating asymptotic giant branch (TP-AGB) stars dominate the flux in some intermediate age populations (Maraston, 2005). We discuss this issue in terms of stellar masses in Conselice et al. (2007) who show that the effects of TP-AGB stars do not kick in until at redshifts higher than the scope of this study ( $z > 2$ ), and thus are not a concern in the present work.

Results are outputted from K-correct for each input pixel, giving rest-frame fluxes at  $NUV, U, B, V, R, I$  magnitudes plus their associated errors, mass-to-light ratios in all of these bands and finally the stellar mass in that pixel. We then reconstruct the image of the galaxy in stellar mass based on these calculations across the galaxy. We use a signal-to-noise limit of  $S/N = 3$  per pixel in stellar mass for all optical bands, for a reliable calculation. We also investigate how the results would change if pixels are summed together, finding similar results with the exception of the asymmetry which tends to decrease at lower resolutions.

#### 3.2 Visual Classifications

We have classified our entire sample visually, using the  $z_{850}$  galaxy images and the object segmentation maps. We have derived the classification system by applying the most appropriate criteria to this particular dataset. The classification scheme is divided into nine categories, ranging from compact objects (spherical with little or no apparent envelopes) to obviously merging systems (with evidence of tidal streams and other merger attributes). Six objects in the catalogue were found to be unresolved and these were removed from the sample. We give a description of these types and how they were selected below. We often refer to these galaxy types throughout this paper, and Appendix B gives a description of these types in terms of our measured indices. Figures 2-10 show examples of these galaxy types.

##### 3.2.1 Compact Ellipticals

The *compact ellipticals*, denoted as ‘‘cE’’, were identified as compact objects that varied smoothly across their radii when viewed morphologically. These objects had little or no sign of an envelope usually associated with early-type galaxies. The compact Es are generally found at lower redshifts, at  $z < 0.4$  with a few between  $0.6 < z < 0.8$ . The dis-

<sup>2</sup> distributed at <http://cosmo.nyu.edu/blanton/kcorrect/>

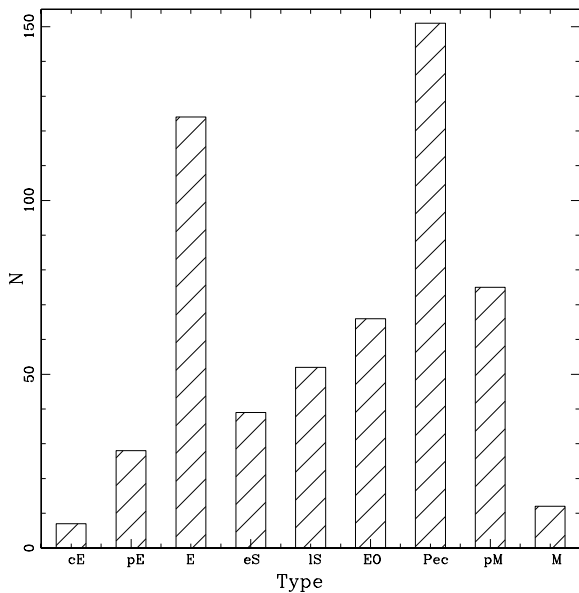


**Figure 1.** The number of galaxies in each of our sample classifications as described in §3.2. Galaxies were visually classified by inspection of both  $z_{850}$  images and segmentation maps.

tinguishing feature of these compact Es is their small sizes, with half-light radii of  $< 1$  kpc.

### 3.2.2 Ellipticals

The elliptical galaxies are amongst the most popular and important galaxy type in our study, as they are typically the most massive galaxies in the local universe. One reason for this is that elliptical galaxies, and massive galaxies in general, are the test-bed for understanding theories of galaxy formation which often have strong predictions for how the most massive galaxies should form (e.g., Bertone & Conselice 2009). The ellipticals we see at high redshift are likely the progenitors of the massive ellipticals found today.

Galaxies with the familiar features of nearby *elliptical galaxies* were classed as such, and given the label “E”. 28 E galaxies were identified, which at first glance have the appearance of early types, but on closer inspection and by varying the image contrast had some peculiar features, such as multiple nuclei or minor disturbances in the internal structure. These objects were classified as *peculiar ellipticals*, and are labelled as pE (Conselice et al. 2007).

### 3.2.3 Spirals/Disks

Objects with a disc-plus-bulge structure were classified as *early-type spirals* (“eS”) if the bulge appears larger than the disc component, and *late-type spirals* (“IS”) if the disc is larger than the central bulge. Edge-on disc galaxies are denoted by “EO”.

The spiral galaxies are amongst the most interesting for this study given that they often contain two major stellar population types segregated spatially. Traditionally this is

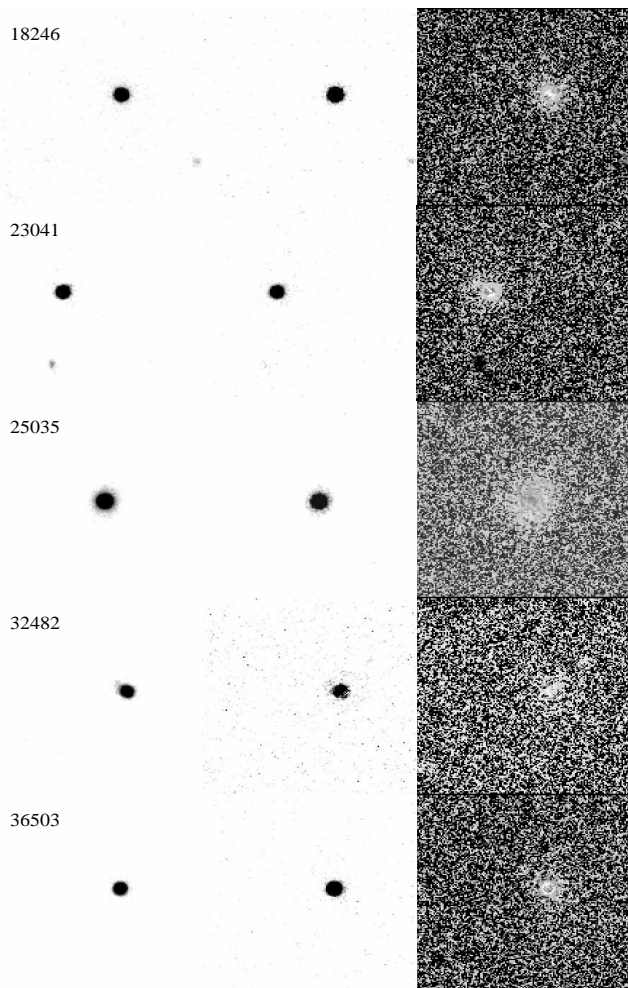


**Figure 2.** Visual displays of the light (in  $z_{850}$ , left), stellar mass (middle) and the distribution of  $M/L$  ratios (right) for the compact elliptical (cE) galaxies. The  $M/L$  map is scaled such that white corresponds to higher  $M/L$  values, and black to lower  $M/L$  values. This convention is used in the following Figures 3 to 10.

seen as an older stellar population making up the bulge, and the spiral arms consisting of younger stellar populations.

### 3.2.4 Peculiars and Mergers

Objects that did not fit easily into any of the previously defined categories, but whose segmentation map showed them to be singular, or unconnected to any apparently nearby object in the image, were classified as *peculiar*, “Pec”. These are galaxies that could possibly have merged in the recent past.

Galaxies whose morphology also ruled them out from any previously defined class but whose segmentation map showed them to be connected to, or associated with, at least one other object on the image, but without obvious merger signatures, were classified as *possible mergers* (“pM”). Galaxies with the pM requirements and which showed obvious signs of merging, such as tidal tails, were classified as *mergers* (“M”).

This information is summarised for quick reference in Table 1. The sample was independently classified four times.

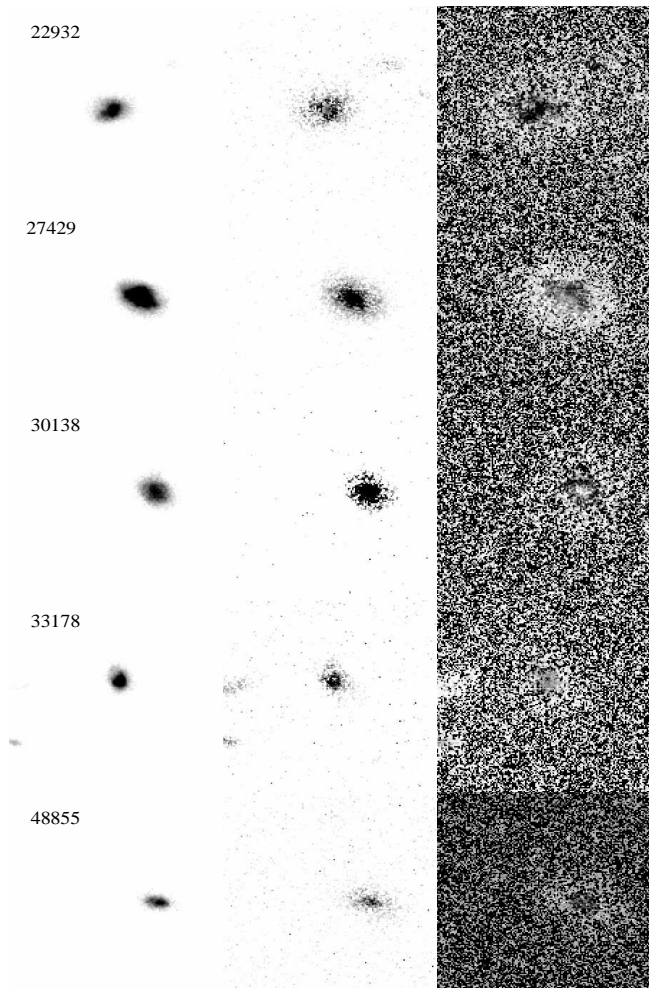


**Figure 3.** Comparing the light (in  $z_{850}$ ), stellar mass maps, and the distribution of  $M/L$  ratios for examples of peculiar elliptical (pE) galaxies. The scale and convention is the same as that used in Fig. 2.

The mode of the results were taken to be the true classification and where an indecisive split was produced the lowest numerically valued type was chosen. Figure 1 shows a histogram of the sample classifications.

We note that there are a significant number of peculiar galaxies in our sample (e.g., Figure 1), much higher than what has been found at lower redshifts in previous work investigating galaxy morphology (e.g., Conselice et al. 2005). These are systems that at lower resolution would be classified as disk-like galaxies in many cases. They are not necessarily merging systems, but are likely normal galaxies in some type of formation, the modes of which are one of the features we investigate later in this paper.

We show examples of each of the above types in Figures 2-10, with five examples shown for each. These figures show the image of the galaxy in the  $z_{850}$ -band, the stellar mass maps, and the mass to light ratio for each galaxy.

### 3.3 CAS Analysis

We use the concentration, asymmetry, clumpiness (CAS) parameters to quantitatively measure the structures of our

Type	Description
E	Elliptical
cE	Compact E
pE	Peculiar E
eS	Early-Type Spiral
lS	Late-Type Spiral
EO	Edge-on disc
Pec	Peculiar
pM	Possible merger
M	Obvious merger

**Table 1.** Descriptions of the classification scheme.

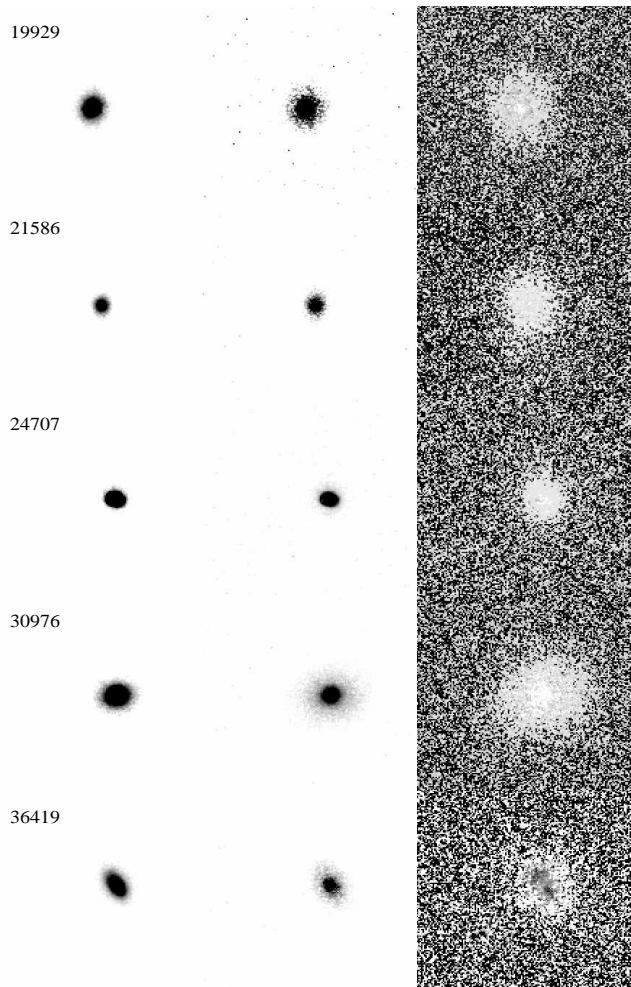


**Figure 4.** Comparing light, stellar mass maps and  $M/L$  for the elliptical (E) galaxies. The scale and convention is the same as that used in Fig. 2.

sample, in all available bands,  $BViz$ , and on the stellar mass maps. We also measure the Gini and  $M_{20}$  parameters, forming an extensive non-parametric method for measuring the structures and morphologies of galaxies in resolved CCD images (e.g., Conselice et al. 2000a; Bershadsky et al. 2000; Conselice et al. 2002; Lotz et al. 2004; Conselice 2003; Lotz et al. 2008). The premise for using these parameters is to tap into the light distributions of galaxies, which reveal their past and present formation modes (Conselice 2003). The re-

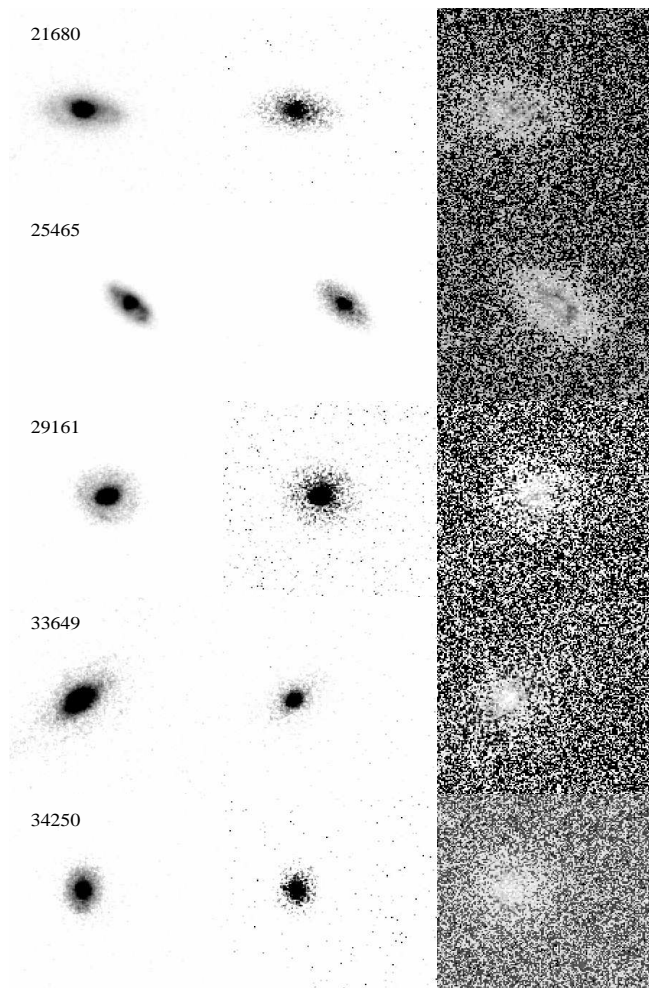


**Figure 5.** Comparing light, stellar mass maps and  $M/L$  for the early-type spiral galaxies (eS). The scale and convention is the same as that used in Fig. 2.

gions into which the traditional Hubble types fall in CAS parameter space is well understood from local galaxy comparisons. For example, selecting objects with  $A > 0.35$  finds systems that are highly disturbed, and nearly all are major galaxy mergers (e.g., Conselice et al. 2000b; Conselice 2003; Hernandez-Toledo et al. 2005; Conselice 2006a). A more detailed analysis of this problem is provided in Appendix A for optical light.

We measure the structural parameters for the GOODS sample using the method of Conselice et al. (2008), with slight adjustments made for the stellar mass maps, to enable the code to handle the large values of stellar masses per pixel, rather than flux. The radius of each individual galaxy within the postage stamp image/mass map is measured on the stellar mass map, and we define all our indices within the Petrosian radii (e.g., Petrosian 1976; Bershady et al. 2000; Conselice 2003). The Petrosian radius has been found to be a better and more reliable radius (and reproducible) than the isophotal radius (Petrosian 1976). The limits and relationship to other radii is described in detail in terms of total light in a galaxy by Graham et al. (2005).

Circular apertures are used for measuring our Petrosian

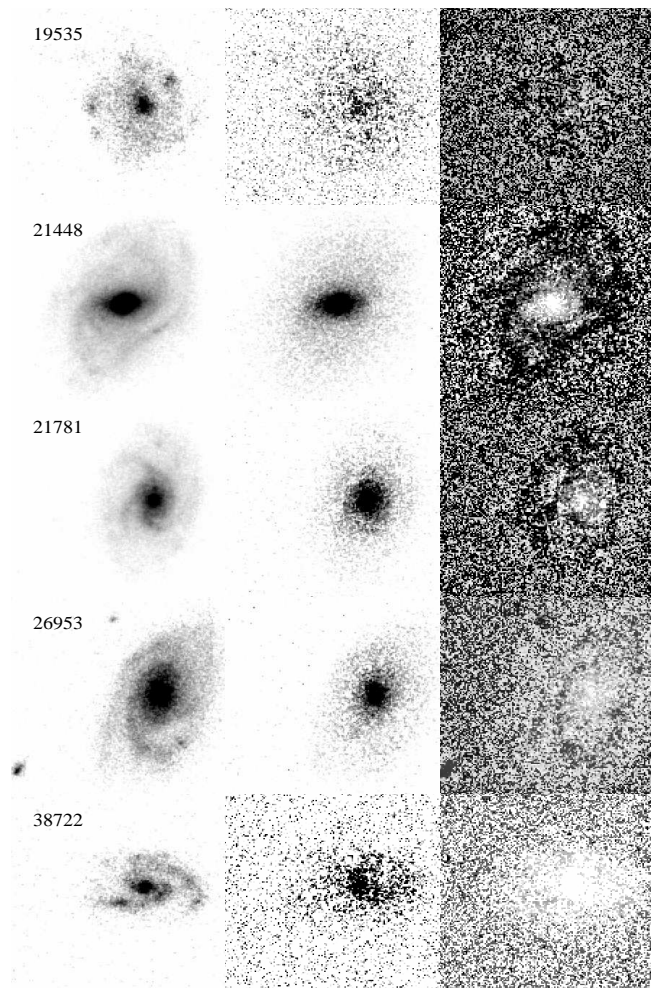


**Figure 6.** Comparing light, stellar mass maps and  $M/L$  for the late-type spiral galaxies (lS). The scale and convention is the same as that used in Fig. 2.

radii and quantitative parameter estimation. The Petrosian radius used to measure our parameters is defined by,

$$R_{\text{Petr}} = 1.5 \times r(\eta = 0.2),$$

where  $r(\eta = 0.2)$  is the radius where the surface brightness (or stellar mass per unit area) is 20 percent of the surface brightness (or stellar mass per unit area) within that radius (Bershady et al. 2000). Note that this is a distance independent measurement, given that surface brightness dimming effects both measurements of surface brightness in the same way.

Accounting for background light and noise is extremely important when measuring structural parameters, especially for faint galaxies, and this must also be dealt with for the stellar mass maps. The measured parameters in the  $B_{435}$ ,  $V_{606}$ ,  $i_{775}$  and  $z_{850}$  bands and stellar mass images are corrected as described in Conselice et al. (2008), by considering a background area close to the object, and the segmentation map of the object. Using a background close to the galaxy itself, any problems introduced by objects imaged on a large mosaic, with a non-uniform weight map, and the object itself being faint compared to the background, are alleviated. We

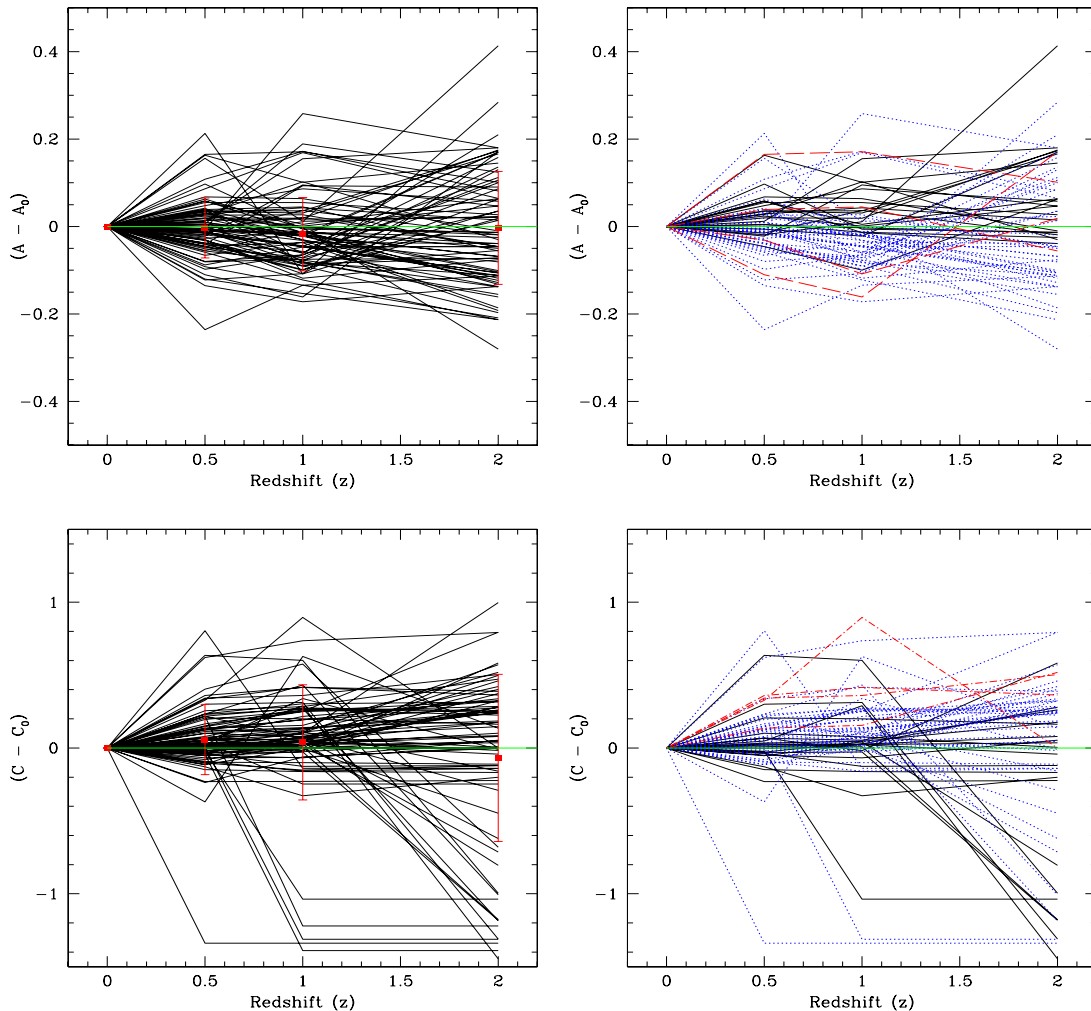


**Figure 11.** The change in the asymmetries and concentrations measured on our stellar mass maps as a function of redshift due simply to distance effects. Show at the top is the change in the asymmetry parameters for a mixture of nearby galaxies of various types: ellipticals, spirals and irregulars, while the bottom two panels are for the concentration index. The left hand side for both shows the change for the entire sample we simulation with the red dots and errorbars showing the average change and  $1\sigma$  variation of that change. The right hand side shows these simulations divided up between ellipticals (black solid line), spiral galaxies (blue dotted line) and irregulars (red dashed line.)

review below how the *CAS* parameters are measured. These are described in more detail in Bershady et al. (2000), Conselice et al. (2000), Conselice (2003) and Lotz et al. (2008).

### 3.3.1 Asymmetry

We measure the asymmetry of a galaxy by taking the original galaxy image (or stellar mass map), rotating it by 180 degrees about its centre, and then subtracting the two images (Conselice 1997), with corrections for background and radius (see Conselice et al. 2000a for details). The centre of rotation is found using an iterative process, which locates the minimum asymmetry. A correction is made within the stellar mass maps for this parameter, as it was found that uncertainties in the mass-to-light ratio adversely affected the asymmetry measurement. We found that approximately 15 percent of the stellar mass in the asymmetry calculation is left over from random fluctuations in  $M/L$ . This was

compensated for including an additional correction for this uncertainty through a slight additional subtraction to the asymmetry signal. This was done by scaling the asymmetric residuals of the rotated and subtracted image by an increase of 15%, that is only 85% of the residual is considered.

We measure the background light in the same way as for the light measures of asymmetry, although because we are dealing with a conversion to stellar mass, which is not trivially done for the background, we have some background values which are lower than zero. To deal with this, we placed all the negative pixels in the stellar mass map background to zero.

The equation for calculating asymmetry is:

$$A = \min \left( \frac{\sum |I_0 - I_{180}|}{\sum |I_0|} \right) - \min \left( \frac{\sum |B_0 - B_{180}|}{\sum |I_0|} \right) \quad (3)$$

Where  $I_0$  denotes the original image pixels,  $I_{180}$  is the image after rotating by  $180^\circ$ . The background subtraction is

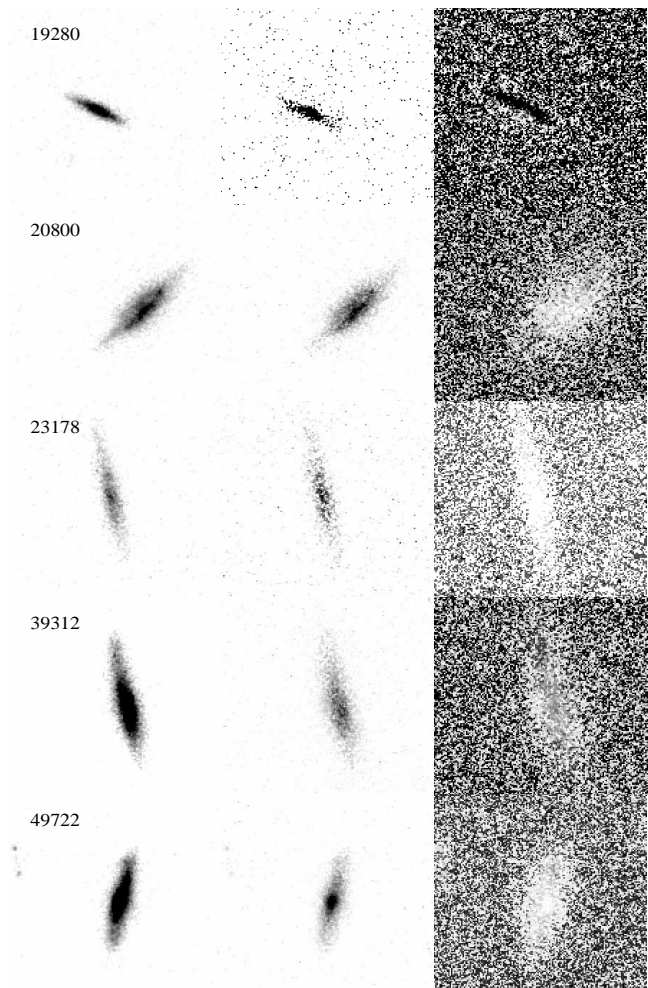


**Figure 7.** Comparing light, stellar mass maps and  $M/L$  for the edge-on disk galaxy (EO) galaxies. The scale and convention is the same as that used in Fig. 2.

made using light (or mass) from a blank sky area,  $B_0$ , and is minimised using the same process as for the object itself. The higher the values of  $A$ , the higher the degree of asymmetry the galaxy possesses, the most extreme cases usually corresponding to merger candidates (Conselice 2003).

### 3.3.2 Concentration

The concentration parameter measures the the intensity of light (or stellar mass) contained within a pre-defined central region, compared to a larger region towards the edge of the visible galaxy. Concentration is most often defined as the ratio of the flux contained within circular radii possessing 20 percent and 80 percent ( $r_{20}$ ,  $r_{80}$ ) of the total galaxy flux,

$$C = 5 \times \log \left( \frac{r_{80}}{r_{20}} \right). \quad (4)$$

A higher value of  $C$  corresponds to an object where more light is contained within the central region. This measurement has been shown to correlate with the halo, and total stellar masses, of nearby galaxies (e.g. Bershady et al. 2000; Conselice 2003).

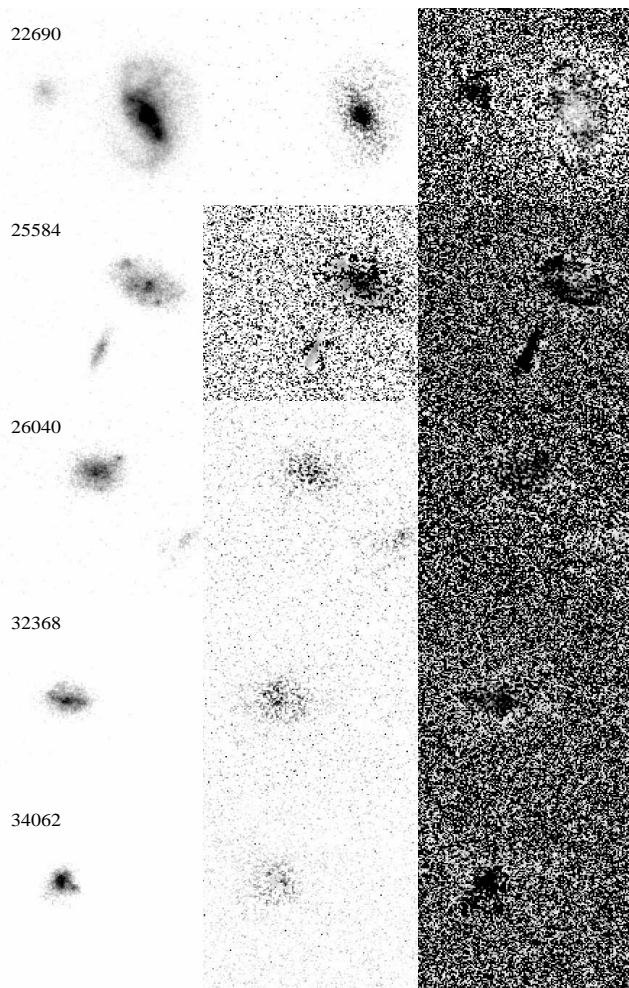


**Figure 8.** Comparing light, stellar mass maps and  $M/L$  for the peculiar (Pec) galaxies. The scale and convention is the same as that used in Fig. 2.

### 3.3.3 Clumpiness

Clumpiness ( $S$ ) is related to asymmetry, in that it is used to measure the amount of light (or mass) in a galaxy that exists in discrete, clumpy distributions. In this definition, a smooth galaxy contains light at low spatial frequencies, such as elliptical galaxies, whereas clumpy systems have most of their light contained in high spatial frequencies. Star forming galaxies tend to be clumpy in structure, with high  $S$  values. We measure clumpiness via:

$$S = 10 \times \left[ \left( \frac{\Sigma(I_{x,y} - I_{x,y}^\sigma)}{\Sigma I_{x,y}} \right) - \left( \frac{\Sigma(B_{x,y} - B_{x,y}^\sigma)}{\Sigma I_{x,y}} \right) \right], \quad (5)$$

where, the original image  $I_{x,y}$  is blurred to produce a secondary image,  $I_{x,y}^\sigma$ . The secondary image is subtracted from the original image to create a residual map, showing only the high frequency structures contained within the galaxy (Conselice 2003). The residuals are quantified by normalising, using the total light in the original galaxy image, and then subtracting the normalised residual sky. The smoothing kernel,  $\sigma$ , used is determined from the radius of the galaxy, and has the value  $\sigma = 0.2 \cdot 1.5 \times r$  ( $\eta = 0.2$ ) (Conselice 2003). The centres of the galaxies (roughly the inner 1/10th the

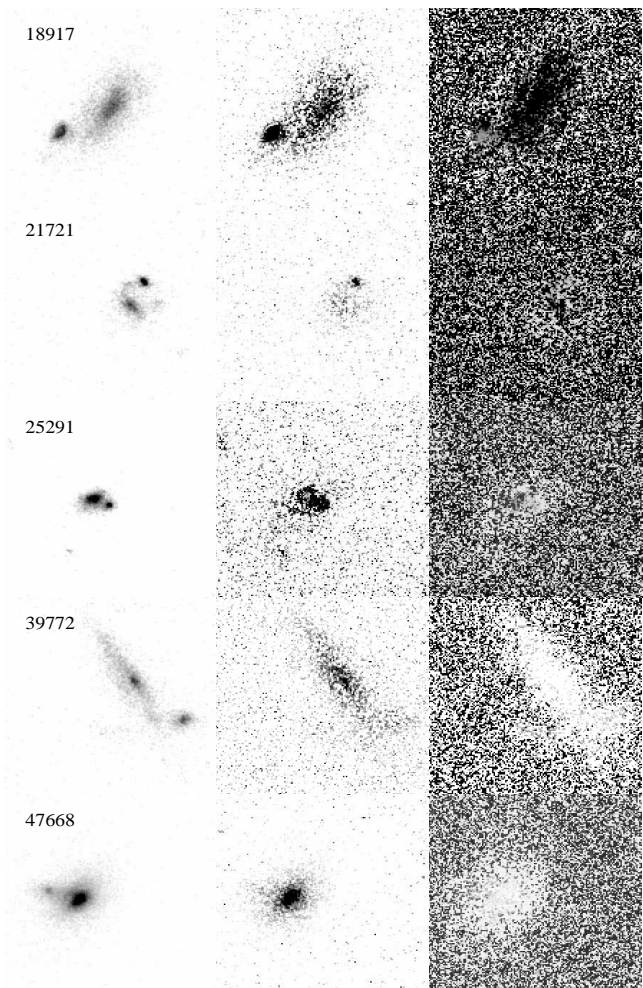


**Figure 9.** Comparing light, stellar mass maps and  $M/L$  for the possible-merging (pM) galaxies. The scale and convention is the same as that used in Fig. 2.

Petrosian radius) are removed during this procedure. This parameter is furthermore the most difficult to measure and is best measured on galaxies imaged with a high S/N ratio, and are only of limited use in this paper. Also, the Clumpiness is highly sensitive to resolution or seeing, although the ACS imaging we use at these redshifts is within the range where values can be properly compared to nearby calibration data sets (Conselice 2003).

### 3.3.4 Gini

The Gini coefficient ( $G$ ) is defined through the Lorentz curve of the light distribution and does not depend on a predefined central position, thus distinguishing it from the concentration parameter. If  $G$  is zero, the galaxy has a uniform surface brightness, whereas if a single pixel contains all the flux,  $G$  is unity. To calculate  $G$  efficiently, the pixel flux (or stellar mass) values,  $f_i$ , are sorted into increasing order and the following formula is used:

$$G = \frac{1}{|f|n(n-1)} \sum_i^n (2i - n - 1) |f_i| \quad (6)$$

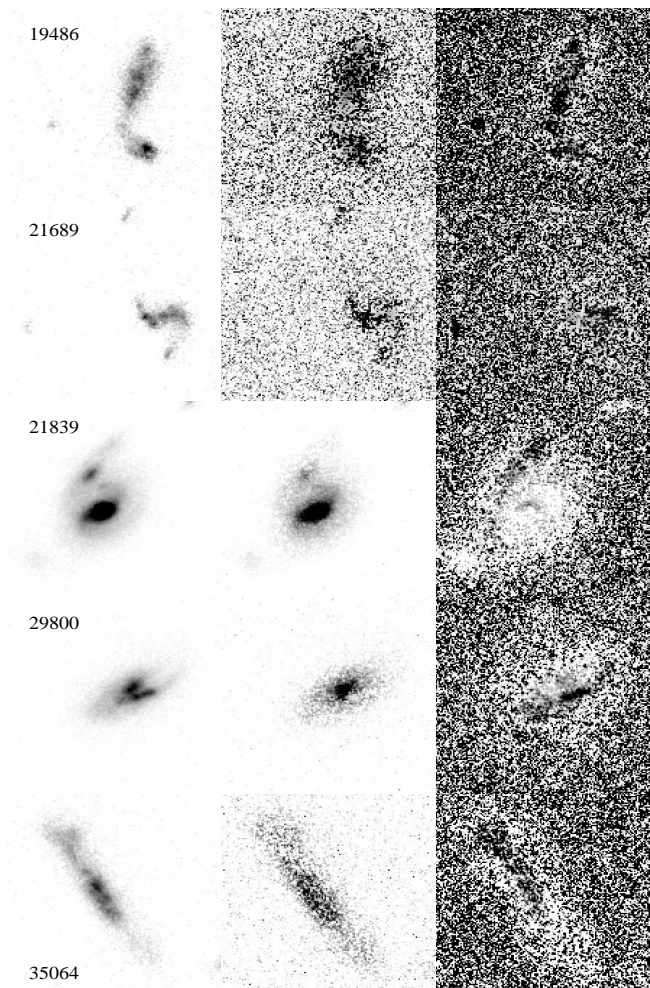


**Figure 10.** Comparing light, stellar mass maps and  $M/L$  for the merging (M) galaxies. The scale and convention is the same as that used in Fig. 2.

where  $n$  is the total number of pixels in the galaxy (Lotz et al. 2004, 2008).

### 3.3.5 $M_{20}$

$M_{20}$  is anti-correlated with concentration such that galaxies with high concentration have low  $M_{20}$  values.  $M_{20}$  is a direct tracer of the brightest regions in a galaxy, but does not require a pre-determined central coordinate, rather this is calculated to be the location of minimal  $M_{20}$ .  $M_{20}$  is more sensitive to merger signatures than concentration and is normalised by the total moment of the galaxy. It is defined as

$$M_{20} \equiv \log_{10} \left( \frac{\sum_i M_i}{M_{tot}} \right), \text{ while } \sum_i f_i < 0.2 f_{tot} \quad (7)$$

$$M_{tot} = \sum_i^n M_i = \sum_i^n f_i [(x_i - x_c)^2 + (y_i - y_c)^2] \quad (8)$$

where  $x_c, y_c$  is the galaxy centre (Lotz et al. 2004).

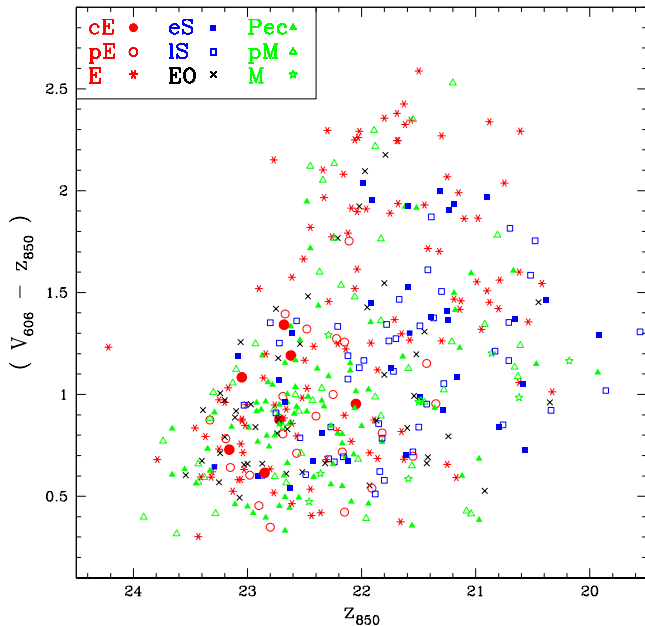


**Figure 12.** The colour-magnitude relation for our sample of galaxies. Displayed is the  $(V_{606} - z_{850})$  colour vs. the magnitude of the galaxy as observed in the  $z_{850}$  band. Different galaxy types are displayed, including: compact ellipticals (cE), peculiar ellipticals (pE), ellipticals (E), early-type spirals (eS), late-type spirals (IS), edge-on disk galaxies (EO), peculiar galaxies (Pec), possible-merger galaxies (pM) and merging systems (M). This key is used throughout the remainder of this paper.

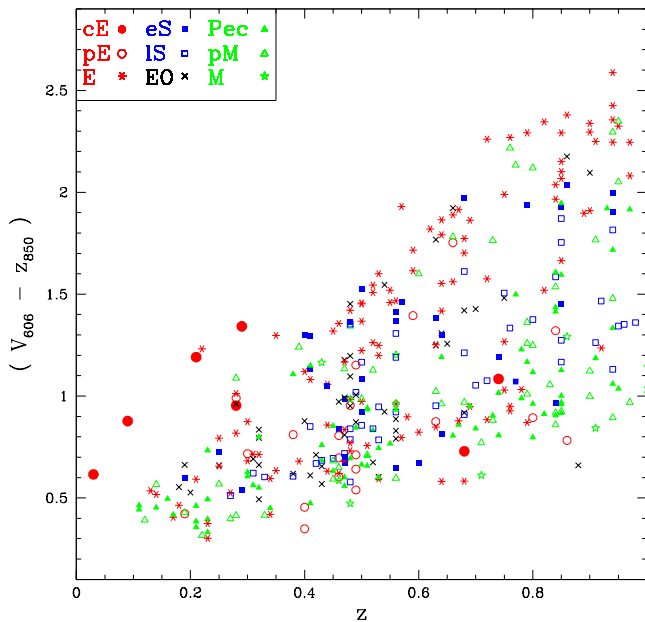


**Figure 13.** Colour in observed  $(V_{606} - z_{850})$  vs. Redshift ( $z$ ) for our sample. The points displayed are the same as in Fig. 12.

### 3.4 Simulations of CAS parameters

One issue that we must address within this paper is how well we are measuring structure on the stellar mass maps for our sample of galaxies, and importantly how the measurement of stellar mass structure would change with redshift due only to cosmological effects. This is critical if we are to make any inferences of the evolution of galaxies in terms of their stellar mass distribution over time. This issue has been addressed before for visual images of galaxies in Conselice (2003) and in Beauvais & Bothun (1999) for velocity fields in spiral galaxies. Here we address it for the stellar mass maps.

We simulate how our stellar mass map creation process, and CAS measurements would vary as a function of redshift due to a decrease in the signal to noise and resolution. We carry out this process in the same way we have for the actual galaxies in the GOODS fields that we analyse in this paper. We take a sample of 82 nearby galaxies of various types - ellipticals, spirals, and irregulars, convert their flux values to stellar mass. We also go through the entire process we do on GOODS, including setting equal to zero the background values with negative stellar masses.

This stellar mass conversion is done after the galaxy is redshifted, so that we are mimicking as much as possible how the real observations and measurements are done. The simulation itself is done by simulating each image at some redshift  $z_1$  to how it would appear at  $z_2$ , with  $z_2 > z_1$ . In our case  $z_1 \sim 0$ . When carrying out these simulations of placing lower redshift galaxies to high redshifts we calculate first the rebinning factor,  $b$ , which is the reduction in apparent size of a galaxy's image when viewed at higher redshift. The other major factor is the relative amounts of flux from the sky and galaxy, and the noise produced from the galaxy, sky, dark current, and imaging instrument (e.g., read noise) from ACS. The process and details for how these simulations are done can be found in Conselice (2003).

In summary, the surface brightness of the simulated image must be reduced such that the equation,

$$4\pi\alpha_{z_1}N_{z_1}p_{z_1}(1+z_1) = 4\pi\alpha_{z_2}N_{z_2}p_{z_2}(1+z_2)\frac{\Delta\lambda_{z_1}}{\Delta\lambda_{z_2}}, \quad (9)$$

holds, whereby the galaxy as observed in one filter, and is simulated in another with central rest-frame wavelengths of  $\lambda_{z_1}$  and  $\lambda_{z_2}$  and widths  $\Delta\lambda_{z_1}$  and  $\Delta\lambda_{z_2}$ . In the above equation  $N_z$  is the total number of pixels within the galaxy at  $z$  and  $p_z$  is the average ADU counts per pixel. The calibration constant  $\alpha_z$  is in units of  $\text{erg s}^{-1} \text{cm}^{-2} \text{\AA}^{-1} \text{ADU}^{-1}$ .

A sky background, and noise from this backgrounds is added to these images by  $B_z \times t_z$ , where  $B_z$  is background flux in units of in units of  $\text{ADU s}^{-1}$ . For ACS simulations we take these values from the measured background based on GOODS imaging (Giavalisco et al. 2004) checked to be consistent with the values from the ACS handbook. Other noise effects are then added, including read-noise scaled for the number of read-outs, dark current and photon noise from the background. Our resulting images are then smoothed by the ACS PSF as generated by Tiny-Tim (Kriss et al. 2001), although using PSFs measured from stars give the exact same results.

From these simulated images at redshifts  $z = 0.5, 1$  and  $2$ , we then reconstruct the stellar mass images in the same way as we do for our original galaxies, and then measure the

CAS parameters on these stellar mass images. The results of this are shown in Figure 11 for the concentration and asymmetry parameters. The  $M_{20}$  and Gini parameters however have similar behaviours, as do the galaxy half-light radii. We find that the clumpiness indices have a similar average difference, but with a much larger scatter.

What we find overall is that the trend with redshift is such that the concentration and asymmetry parameters on average do not change significantly when measured in stellar mass (Figure 11). We show in the right panel of Figure 11 the change in  $C$  and  $A$  when divided into early/late/peculiar types. Again, on average there is not a significant change with redshift, although individual galaxies clearly can have significant differences at higher redshift.

We also investigate how our parameters change at each redshift between the stellar mass and the visual images after the simulation. We find very little difference except that at the highest redshifts of our simulations, at  $z = 2$ , we find that the average change in the asymmetry parameter changes  $\delta A = (A_{\text{opt}} - A_{\text{mass}}) \sim -0.1$ , such that the stellar mass image is more asymmetric than the optical light one. We also investigate the same quantities that we use in later figures, finding that twice the difference in the asymmetries of the optical and stellar mass image, divided by the sum of these, increases steadily until it reaches a values of  $-1.1$  at  $z = 2$  similar to what we see later in this paper for the actual values. However at  $z = 1$  we find that this change is less and closer to  $-0.1$ .

## 4 ANALYSIS

The following sections describes the analysis of our sample, and what we can learn from examining their structures in stellar mass maps, and how this evolves over time. We first examine the distribution of visual classifications for our sample and their global colours. We later describe the stellar mass maps we construct for these galaxies, and then finally present a structural analysis of these systems based on the distribution of their stellar mass.

### 4.1 Global Properties of the Sample

In Figure 12 we show the observed colour magnitude diagram for our sample. Each morphological class is plotted as a different symbol; solid red circles represent the cE's, open red circles show the pE galaxies and the E galaxies are represented by red stars. Solid blue squares show the eS and open blue squares the lS systems. Edge-on disk galaxies are represented by black diagonal crosses and solid green triangles show the Pec systems. pM and M galaxies are represented by open green triangles and open green stars respectively. This key is used throughout the rest of the paper in the various figures.

Based on this, we find that our classified early-type galaxies are on average redder and brighter than the peculiars and pM/M systems, while the spirals tend to be bluer across a range of brightnesses, but the differences are not so clear as would be expected for a sample at low- $z$  only. This colour-magnitude diagram does not show such an obvious morphological sequence as is seen for purely Hubble type galaxies in the nearby universe (e.g., Conselice 2006b).

The relation between  $(V_{606} - z_{850})$  colour and redshift is shown in Figure 13. The symbols are the same as those in Fig. 12. As can be seen, there is a general trend for all types to become redder with increasing redshift, which is an expected feature of redshift. The early types are reddest across the whole redshift range, followed by the eS and lS galaxies, with the Pec/pM/M systems the bluest across all redshifts. The compact ellipticals are blue and faint. Note however that some pM and eS galaxies are quite red. What this reveals is that there is a decoupled relation between the colour and morphologies of galaxies not seen in nearby galaxies where this correlation is strong. A specific morphological type as measured visually at high- $z$  cannot be used to predict the colour of the galaxy.

### 4.2 Stellar Mass and Mass to Light Ratio Maps

By calculating stellar mass to light ratios and the stellar mass within each pixel of each galaxy image in our sample, we reconstruct the image of each galaxy in terms of stellar mass and mass-to-light ratio. We do this for each galaxy, using the method described in LCM07, and present five representative examples for each classification in Figures 2 to 10. This figures present galaxy images in  $z_{850}$  (left), stellar mass (centre) and  $(M/L)_B$  (right), which we discuss below. The images are grey-scaled such that the darkest pixels represent those brightest in  $z_{850}$ , and those that are most massive. In the mass-to-light image, the whitest pixels are those with the highest  $(M/L)$ , or redder in colour. We explain below how these maps appear for our various types.

#### 4.2.1 Compact Ellipticals

Figure 2 shows five examples of the compact elliptical (cE) population in the sample. These galaxies appear similar in their stellar mass maps as they do in their  $z_{850}$  images at first glance. The mass-to-light maps are not as uniform, and there are important quantitative differences between the stellar mass and light images. For example, the galaxy 18246 appears to have a relatively higher  $(M/L)$  in its core compared to its outer parts, whilst galaxy 25035 appears to have a low  $(M/L)$  in its centre, suggesting that it has a bluer core, likely due to star formation. Galaxy 36503 contains a high  $(M/L)$  ring surrounding a blue core.

#### 4.2.2 Peculiar Ellipticals

Five examples of the peculiar elliptical (pE) galaxies are displayed in Fig. 3. These galaxies appear more diffuse in stellar mass than in  $z_{850}$ , in part due to the loss in contrast in the stellar mass maps, but also due to their blue inner colours (Fig. 3). As can be seen in the  $(M/L)$  ratio maps of these galaxies, they have blue cores, and the effect is most pronounced in 22932 and 27429. These galaxies also have blue overall colours compared to pure E galaxies (Fig. 13). These peculiar ellipticals have been seen and studied before in papers such as Conselice et al. (2007). They generally have a high asymmetry, and are found amongst the most massive galaxies in the universe at  $z \sim 1$ . As can be seen in the M/L maps for these systems (Fig. 3), these galaxies also have a diversity in how young and old stellar populations,

including dust, are distributed in these systems compared to normal elliptical galaxies.

#### 4.2.3 Ellipticals

Figure 4 presents five examples of early-types from our sample. These galaxies appear more diffuse and more distributed spatially in their stellar mass than in the  $z_{850}$  band, especially at large radii. These galaxies have larger ( $M/L$ ) ratios in their centres, except for 36419, which is blue, and has a more complicated structure in ( $M/L$ ) than the others. Overall, the E galaxies morphologically have very similar structures in stellar mass and  $z_{850}$ .

#### 4.2.4 Spirals

Figures 5 and 6 show the  $z_{850}$ , stellar mass and ( $M/L$ ) maps for the early-type, and late-type spirals. As found in LCM07, structures within discs, including prominent spiral arms, are often (but not always) smoothed out in stellar mass. This is true for early types as well as late-type spirals, as can be seen for example in galaxy 25465 (Fig. 5). Inspection of the ( $M/L$ ) maps reveal that the discs of many spirals are bluer than their bulges, as expected.

The mass-to-light ratio maps of the edge on galaxies (Fig. 7) are mostly homogeneous in structure. However, the maps of 19280, 39312 and 49722 all show some patches of low  $M/L$ . Indeed, 19280 appears to be blue across the whole image, which would imply that the dust content of this galaxy is low, which is unusual for edge-on galaxies.

#### 4.2.5 Peculiars & Mergers

Figure 8 shows the F814W images, stellar mass maps and  $M/L$  ratio maps for the Peculiar galaxies within our sample. The Peculiar galaxies 22690 and 25584 (Fig. 8) appear to contain objects near the primary galaxy, but in both cases it is the larger galaxies on the right that is the target. Although 22690 looks disturbed in  $z_{850}$ , the effect of smoothing in the stellar mass map is also seen here. This indicates that disturbed regions of the galaxy are due to star forming regions. The  $z_{850}$  image of 22690 does not have the regular morphology of a nearby spiral galaxy, although the stellar mass map has a structure one would expect of such a galaxy, having a central bulge surrounded by a smooth disc. The ( $M/L$ ) map also shows a red central region surrounded by bluer pixels.

The mass-to-light maps of the Peculiars generally show that they are blue and also difficult to see in stellar mass, due to their low mass to light ratio. This suggests that star formation itself might be difficult to trace in stellar mass. However, the stellar mass in the pM galaxy 18917 (Fig. 9) traces the light in the galaxy, despite having a low ( $M/L$ ). Note also that the peculiars are often peculiar spirals, in the sense that they look like nearly normal spirals, but with some peculiar features. Often these peculiars are quite small as well, and many of them are very likely spirals in some type of formation.

The merging galaxy system 21839 (Fig. 10) is similar in stellar mass to its  $z_{850}$  image, but possesses a more intricate structure in ( $M/L$ ). The mass-to-light map shows

the smaller merging object to be blue, whereas the brighter galaxy appears more red but with blue regions in its core.

The system 29800 (Fig. 10), whilst clearly appearing to be a merger between two galaxies of approximately equal brightness in  $z_{850}$ , would likely be classified as a disc galaxy in stellar mass. The bottom of the two bright nuclei has disappeared completely in the stellar mass image, although it is visible as a low ( $M/L$ ) patch in the mass-to-light map.

### 4.3 Comparison Between Galaxy Properties in Mass and Light

In this section we compare how the distribution of stellar mass in a galaxy compares to the distribution of light as seen in the  $z_{850}$  ACS imaging. One of our goals is to determine how appropriate studies in  $z_{850}$  and similar red bands are for measuring the mass content and structure of a galaxy, and how stellar mass quantitative morphologies differ from those measured in light.

In this section we investigate the relationship between galaxy properties in stellar mass and  $z_{850}$ -band light. For galaxy size (as measured by the half-light radius) and the *CAS* parameters we plot the normalised difference between  $z_{850}$  and stellar mass versus the mean value of  $z_{850}$  and stellar mass as a representative figure to determine how these various quantities change.

#### 4.3.1 Galaxy Half-light and Half-mass Radii

One of the basic features of a galaxy is its size, which in this paper we quantitatively mean the half-light radii. Galaxy half-light radii are found to strongly evolve with time, such that galaxies at higher redshifts have a more compact structure (e.g., Ferguson et al. 2004; Trujillo et al. 2007; Buitrago et al. 2008; Carrasco et al. 2010). However, every size measurement has been carried out through measurements of light, and it is desirable to determine how the half-mass radii of galaxies measured in stellar mass maps compares with half-light radii measured using light.

As such, we have calculated half-light (or half-mass) radii ( $Re$ ), in kpc, for our sample in both stellar mass and  $z_{850}$  light, and investigate whether half-light/mass radii are comparable. We define the normalised size difference as

$$2[Re(z_{850}) - Re(M_*)]/[Re(z_{850}) + Re(M_*)],$$

and the average size as

$$\frac{1}{2}[Re(z_{850}) + Re(M_*)].$$

We use these two calculations so as to avoid biasing the analysis when the values become very small in either the stellar mass image, or in the  $z_{850}$  band. We plot the relation between these values in Figure 14. The horizontal dashed line marks the position of equal size ( $Re(z_{850}) = Re(M_*)$ ). The symbols are the same as in Figure 12, and the average dispersion for the sample is represented by the black square points on the right of the plot. The larger black square points in the figure show the average values and the measured dispersion for the ranges of  $\frac{1}{2}(Re(z_{850}) + Re(M_*))$  between zero and one kpc, one and two kpc, up to six kpc. This convention

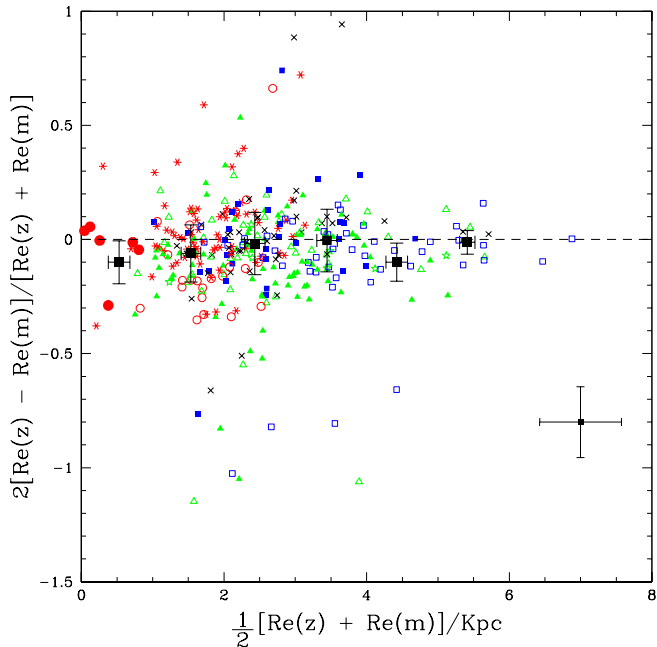


**Figure 14.** Normalised effective-radius difference vs. mean effective radius of the sample in  $z_{850}$  and stellar mass. The error bar to the right of the plot shows the average dispersion for the whole sample. The large black squares denote the average values in equally spaced bins of mean size, with error bars showing the dispersions of these values. This convention is used in all of the parameter comparison plots. The symbols plotted here are the same as in Figure 12.

is used for each of the parameter comparisons in Sections 4.3.2 to 4.3.6.

We note that there is a steady progression for increasing average galaxy size with morphology, from the compact ellipticals, early types and early spirals to the late-type spirals, with the peculiars and edge-on galaxies being more randomly distributed. The points are scattered about the line of equality such that nearly half (42 percent) of the galaxies have  $Re(z_{850}) > Re(M_*)$ . There is, therefore, a slight tendency for sizes in masses to be higher, but this does not vary significantly with average galaxy size and type (see Table 2).

There is no clear tendency for any particular morphological type to be larger in either the  $z_{850}$  or stellar mass image, which suggests that there is no bias introduced by using measurements in  $z_{850}$  band data for size measurements (Trujillo et al. 2007; Buitrago et al. 2008). Table 2. shows that the average difference between the sizes in the stellar mass maps and the  $z_{850}$ -band image is essentially zero, demonstrating that the measurements of half-radii in light does not differ significantly from the measurements in the distribution of stellar mass.

We also examine the normalised difference in size against  $(V_{606} - z_{850})$  colour to test whether there is a tendency for bluer galaxies to have larger radii in stellar mass than in light. This is what we might expect to find if star formation dominated the light near the centre of the galaxy. While, on average, colour does not change with size difference, we find that extreme half-radii differences between stellar mass and  $z_{850}$  are mostly in blue systems.

Type	Mean Size (kpc)	Normalised Size Difference
cE	$0.6 \pm (0.3)$	$0.14 \pm (0.24)$
pE	$1.8 \pm (0.2)$	$-0.11 \pm (0.11)$
E	$1.8 \pm (0.3)$	$0.05 \pm (0.11)$
eS	$2.6 \pm (0.4)$	$0.00 \pm (0.12)$
IS	$3.7 \pm (0.6)$	$-0.10 \pm (0.12)$
EO	$2.7 \pm (0.5)$	$0.02 \pm (0.13)$
Pec	$2.6 \pm (0.5)$	$-0.09 \pm (0.13)$
pM	$2.7 \pm (0.6)$	$-0.07 \pm (0.13)$
M	$3.0 \pm (0.6)$	$-0.08 \pm (0.03)$

**Table 2.** Comparisons between mean  $z_{850}$ -stellar mass half-mass radius ( $R_e$ ) and normalised size difference in  $z_{850}$  and stellar mass, organised by morphological type.

#### 4.3.2 Concentration

Analogous to the galaxy size comparison in the previous section, we compare the concentration parameter in  $z_{850}$  and stellar mass images, as plotted in Figure 15. The dashed line shows  $C(z_{850}) = C(M_*)$  and the black square points represent the average values in equally spaced bins of average concentration.

The average concentration, in both  $z_{850}$  and stellar mass, is generally high for the early types, and lower in the late-types and peculiars, with the early-type spirals being spread between low and high values. The compact elliptical galaxies have a low average concentration, due to the light being spread evenly across a galaxy's pixels.

The average trend shows that the ratio  $\frac{R_{80}}{R_{20}}$  is slightly lower in the stellar mass maps for the early types compared to the  $z_{850}$  band concentration. We find that in general  $R_{80}$  is lower and  $R_{20}$  is higher, compared to those in the  $z_{850}$ -band image, although the effect is mostly due to a smaller  $R_{80}$  although this effects is quite small. It is possible that stellar mass is less centrally concentrated towards the centre of the galaxy in the early-types (raising  $R_{20}$ ), and/or the stellar mass is more diffuse at larger radii than the distribution of light (lowering  $R_{80}$ ). It is also the case that for many galaxies more star formation is seen in the outer regions of the galaxies in the  $z_{850}$ -band, but these pixels are less dominant in stellar mass, raising the value of  $R_{80}$  creating higher values of  $C$  as seen.

#### 4.3.3 Asymmetry

Before we discuss the comparison of our stellar mass map asymmetry values to the  $z_{850}$ -band asymmetries, we note a few things. First, the lowest asymmetry values for the sample are negative in all bands, mainly due to the background correction which for very symmetric galaxies will sometimes be larger than the asymmetry in the galaxy itself. This has the effect, as seen in Figure 16, of skewing the low average asymmetry values differences for the smallest stellar mass measured asymmetries. As can be seen in Figure 16, except for these galaxies with low asymmetry values, there is a clear tendency for galaxies to be more asymmetric in stellar mass than in  $z_{850}$ , this being the case for a large fraction of the non-early type sample. The stellar mass maps also have a

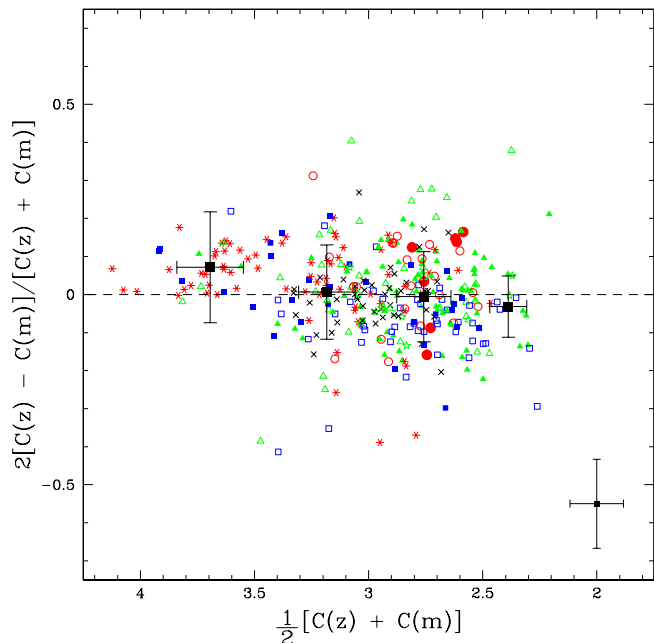


**Figure 15.** Comparison between the concentration parameter in the  $z_{850}$  band and within stellar mass maps. The error bar to the right of the plot shows the average dispersion for the whole sample. The large black squares denote the average values in equally spaced bins of mean concentration, plus dispersions. The symbols used here are the same as in Figure 12.

greater spread in asymmetry values than  $z_{850}$ , and this can be more clearly seen in § 4.4.1.

However, we also note that the blue regions of galaxies are not so well traced by the stellar mass maps, and often led to difficulties with the image contrast, making the galaxy features harder to see, as in the case of the late-spiral 19535 (Fig. 6). Further galaxies, such as 38722 (Figure 6), are clearly more asymmetric and lopsided when viewed in the stellar mass band. In this case, it appears that one spiral arm remains while the other disappears.

There are several reasons why the asymmetry value in the stellar mass maps is higher than in the images. First, when calculating  $A$ , noise tends to be magnified due to the process of subtracting images. The simulations discussed in §3.4 show that there is a tendency for the average galaxies to become more asymmetric in stellar mass measurements than in light. This can explain part of this, but we find that the average difference of around  $-1$  in the relative difference is too high to be accounted for solely by these redshift effects. We discuss some of the reasons for why the asymmetries will be higher in the stellar mass maps than in light.

When calculating stellar masses for each pixel we assume that the  $M/L$  ratio is approximately constant in the surrounding pixels. This should be the case for early type galaxies, especially, due to their uniform stellar populations. To test how much this variance in  $M/L$  could be affecting the  $A$  values, we have measured the  $M/L$  pixel variance in a typical early type galaxy (30976, Fig. 4). The mean  $M/L$  for a pixel in this galaxy is  $(M/L)_B = 1.29$  with a typical standard deviation in the surrounding pixels of  $\sigma_{M/L} = 0.27$ . Although a correction has been applied to minimise this ef-

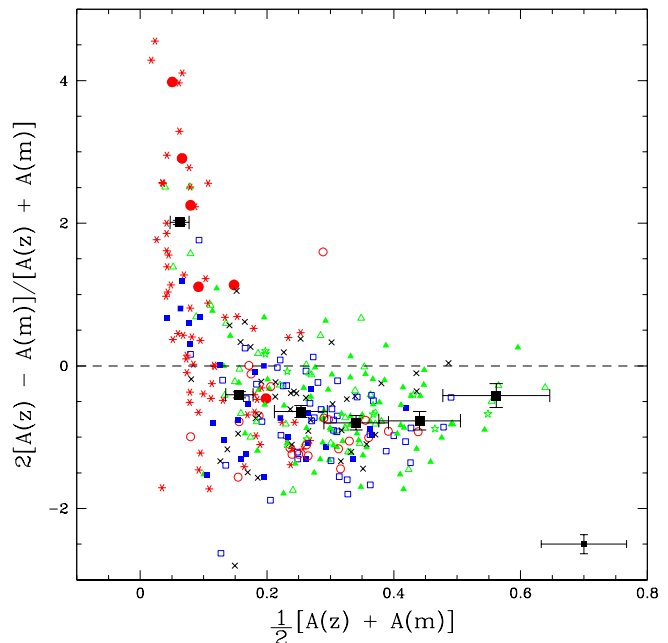


**Figure 16.** Comparison between the asymmetry parameter in  $z_{850}$  and stellar mass. The points and conventions are the same as in Figure 12. Note that the asymmetry in the stellar mass is lower than the  $z$ -band for only the early types. This is due to the method of measuring the asymmetry, where the sky background is handled in a different way than for imaging, resulting in higher values for later type galaxies (§4.3.3).

fect (see §3.3.1), it is not enough to account for the high asymmetry signal in the spiral galaxy stellar mass maps, and thus this asymmetry is likely a real effect due to the nature of the calculation of this parameter, and especially the background, as described in §3.3.1.

To further understand why late-type spiral galaxies are more asymmetric in stellar mass than  $z_{850}$ , we have examined these galaxies in detail and present four examples of the late-type sample in both  $z_{850}$  (Fig. 17), and stellar mass maps. Two of these galaxies have low asymmetries in both stellar mass and  $z_{850}$  (25751 and 21448), and galaxy 21448 in particular, demonstrates the smoothing of spiral arms, which we observed previously in nearby galaxies (LCM08). However, two of these galaxies have higher asymmetries in stellar mass than in  $z_{850}$  (19535 and 34946). Object 19535, especially, shows little relation in stellar mass to the  $z_{850}$  image. The star forming knots and central bulge, which can be seen clearly in  $z_{850}$ , translate to large scale asymmetries in stellar mass. There are several possible explanations for this effect. The star forming regions in 19535 could truly be more massive per pixel than the surrounding disk, due to the high masses and densities of gas and dust required to form such massive star forming regions. This would lead to such regions not being smoothed out in stellar mass, causing higher  $A(M_*)$  values. It is also possible that what we have interpreted as star forming knots in the disk in some cases could be minor merger signatures, that is, low-mass galaxies falling into the object itself.

There is also a trend with morphological-type with increasing asymmetry such that early types have low asym-

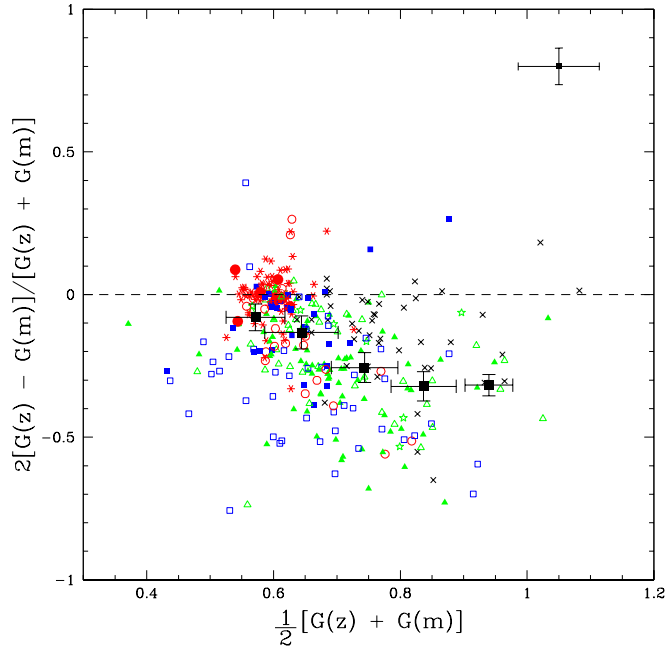


**Figure 18.** Comparison between the Gini parameter in  $z_{850}$  and stellar mass. The points and conventions are the same as in Figure 12.

metry and late-types higher asymmetry. Our findings confirm previous studies who found similar trends (e.g. Conselice et al. 2000). We have also investigated the relation between asymmetry in stellar mass and  $(V_{606} - z_{850})$  colour, and examine this after splitting into two redshift bands:  $z < 0.6$  and  $0.6 \leq z < 1$ . There is a clear trend for galaxies with a higher degree of asymmetry to be blue, with  $\langle (V_{606} - z_{850}) \rangle_{A(M_*) < 0.35} = 1.01(\pm 0.20)$  and  $\langle (V_{606} - z_{850}) \rangle_{A(M_*) \geq 0.35} = 1.22(\pm 0.27)$ . This trend has also been found for asymmetries measured in light (Conselice et al. 2003).

#### 4.3.4 Clumpiness

The clumpiness values in stellar mass maps have a higher degree of uncertainty, as discussed in Section 3.3.3. Overall, we find a trend for clumpiness to be greater in stellar mass than  $z_{850}$ , and this is the case for 91 percent of the sample. However for larger values of average  $S$ , there is a trend such that  $S(M_*) \rightarrow S(z_{850})$ .

The clumpiness parameter is similar to asymmetry, but picks out small scale features, such as compact star clusters, as opposed to large scale asymmetries. It is, therefore, not surprising that uncertainties in  $M/L$  cause a large number of the sample to have  $S(M_*) > S(z_{850})$ , as variations in  $M/L$  from pixel to pixel filter through in the calculation of  $S(M_*)$ . Such variations affect  $A(M_*)$  and  $S(M_*)$  more than the other parameters, as these calculations involve the subtraction of images, which amplifies the  $M/L$  variations and large variations of level within the background.

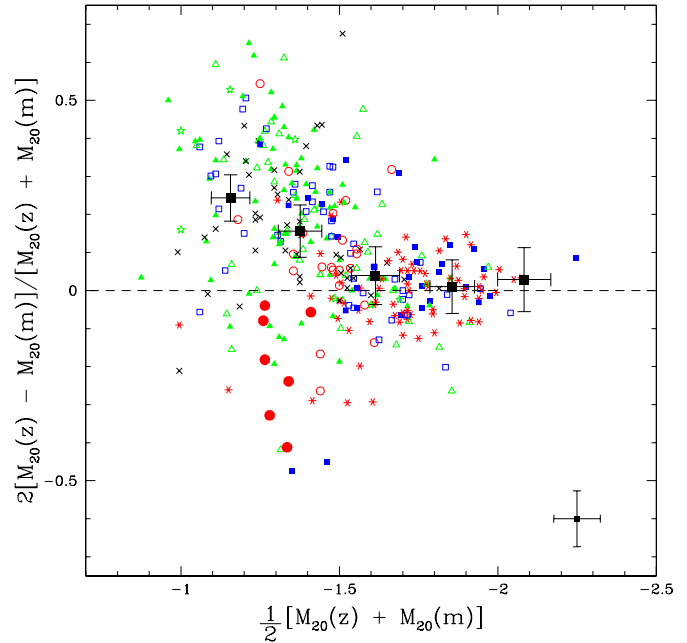


**Figure 19.** Comparison between the  $M_{20}$  parameter in  $z_{850}$  and stellar mass. The points and conventions are the same as in Figure 12. Because of the inverse nature of  $M_{20}$ , galaxies with positive differences on the y-axis are those with more ‘concentrated’ light profiles than in the stellar mass maps.

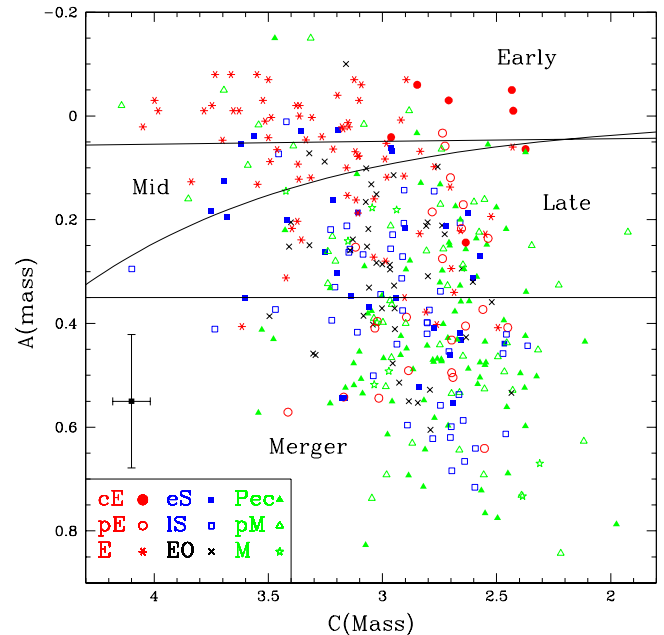


**Figure 21.** The asymmetry-concentration plane for the stellar mass maps. The plotting convention is the same as for Figure 12.

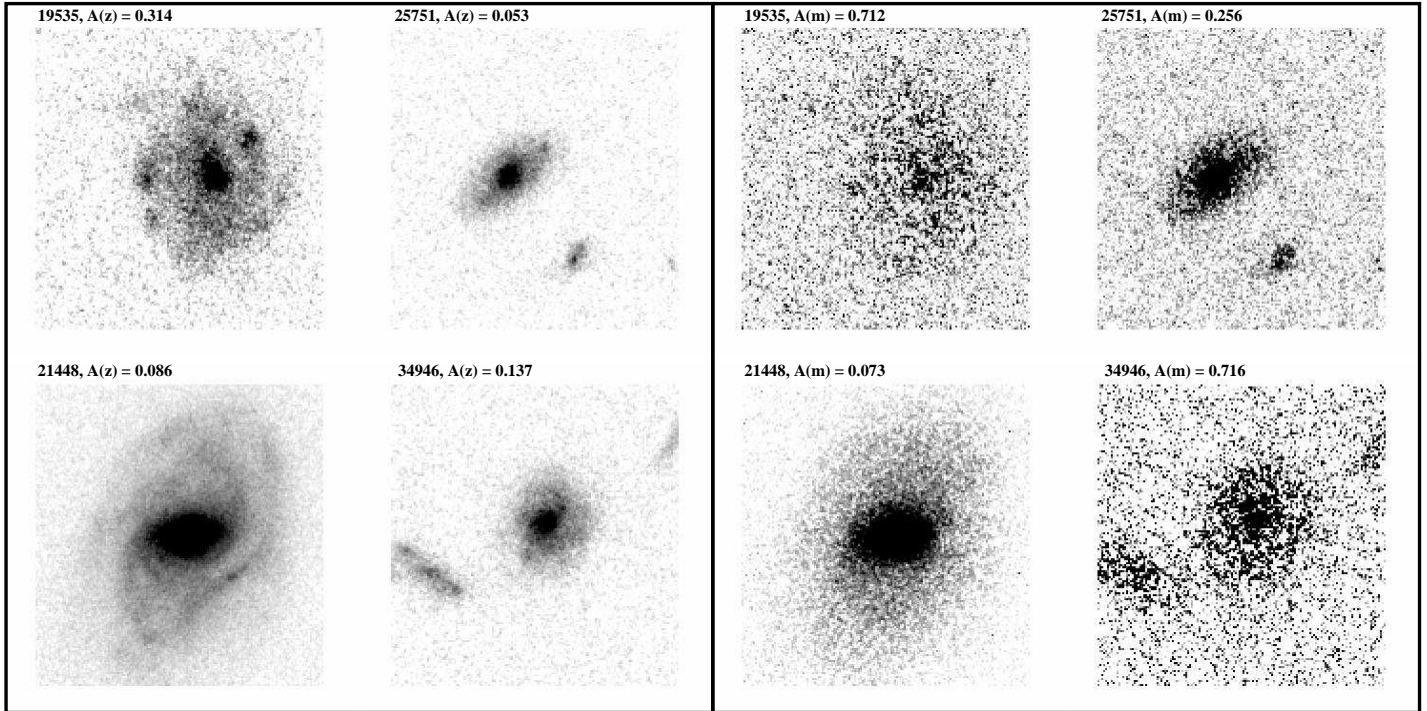


**Figure 17.** Figure showing the  $z_{850}$ -band imaging (left) and stellar mass maps (right) for four late-type spiral galaxies. Each galaxy is labelled with its ID number and  $A(z_{850})$  value. Each image is 4.5 arcseconds on each side. Shown at the top of each image is the ID and the asymmetry parameter measured on the stellar mass maps to be compared with the same value computed in the  $z_{850}$  band.

#### 4.3.5 Gini Index

Figure 18 shows the comparison between the values of the Gini parameter in stellar mass and the  $z_{850}$  band. Although the early-types are more strongly clustered around equality,  $G(M_*) = G(z_{850})$ , there is a clear trend for the sample to have higher  $G$  in stellar mass, with  $G(M_*) > G(z_{850})$  in non-early types within our sample. This comparison of  $G(z_{850})$  and  $G(M_*)$  displays a greater separation between types. The late-type spirals show an approximately even spread in Gini values, from 0.45 to 0.93, but all of these have a higher difference between  $z_{850}$  and stellar mass than the early-types and compact ellipticals.

Figure 18 reveals that the Gini index is higher within the stellar mass maps than in the  $z_{850}$  band, except for early-type galaxies, indicating that most of the stellar mass in later morphological types is contained within fewer pixels within the stellar mass image. This is a significant difference between the early and late-types in our sample. The reason for this is that the bright blue regions of these galaxies vanish as the M/L ratio is inversely proportional to L. This creates effectively a mass distribution with a larger fraction of the mass contained within fewer pixels. For example the bulges become more prominent for the late-type disks while the arms vanish. The bulges in these systems become more prominent and this will rise the value of the Gini index.

What can often be seen in stellar mass maps of late-types and mergers/peculiar is that these bright outer regions vanish, leaving only the central part of the galaxy including most objects in Figure 6 which lose their outer parts and appear almost as early-types. Figure 18 also shows that the Gini index for the early-types in stellar mass and

light are similar, likely because of the small variation in the M/L ratios of the various pixels.

#### 4.3.6 $M_{20}$

We show the differences between the  $M_{20}$  index in the stellar mass maps and the  $z_{850}$  band in Figure 19. Due to the reversed parity in the  $M_{20}$  values, points which lie above the dashed line in Figure 19 have  $M_{20}(M_*) > M_{20}(z_{850})$ , that is, the stellar mass is more diffuse than the light for most systems. This would change however if we used a smaller radius than the standard definition. Overall,  $M_{20}(M_*)$  is higher (less negative) than  $M_{20}(z_{850})$  for most of the sample.

The  $M_{20}$  parameter traces the brightest 20 percent of the flux in the galaxy, or the greatest 20 percent of the stellar mass. This parameter is heavily weighted by the spatial distribution of the most luminous, or most massive, pixels, but is normalised to remove any dependence on galaxy size and total flux/stellar mass.  $M_{20}$ , like  $G$ , is also not dependent on a fixed, pre-determined centre.

Therefore, if stellar mass exactly follows light within a galaxy we would expect that  $M_{20}(M_*) = M_{20}(z_{850})$ . Figure 19 shows that, while this is approximately the case for early-type galaxies and early spirals, the same does not apply for peculiars, late-type spirals and edge-on discs. The compact ellipticals especially differ from this trend, having  $M_{20}(M_*) < M_{20}(z_{850})$ . This is certainly due to the fact that these compact ellipticals have blue cores which render their stellar mass maps more compact in the centre than for galaxies with redder cores.

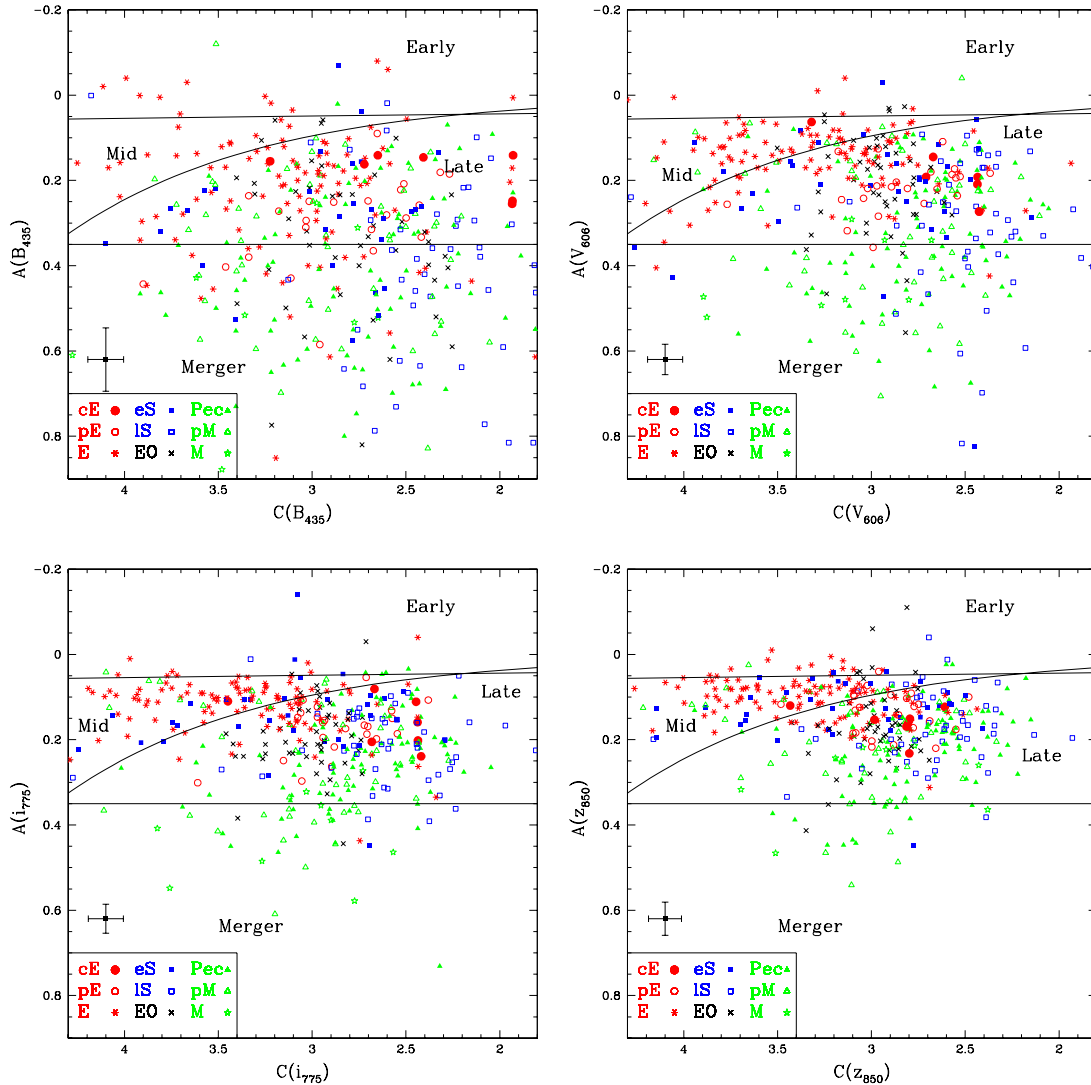


**Figure 20.** Asymmetry vs. concentration in the  $B_{435}$ ,  $V_{606}$ ,  $i_{775}$  and  $z_{850}$  bands. Solid lines show the classification criteria of Conselice (2003). The point in the bottom left segment of the plot shows the average error bar for the whole sample.

## 4.4 Stellar Mass Structure

### 4.4.1 Concentration vs. Asymmetry

We examine how galaxies fall in the classic concentration-asymmetry plane (e.g., Conselice et al. 2000) to determine if different galaxy types, as determined visually, can be better separated at different wavelengths in this parameter space.

We plot the relation between asymmetry and concentration in light for the sample in Fig. 20 and in stellar mass in Fig. 21. Over-plotted are the classification criteria of Conselice (2003) and Bershady et al. (2000). Galaxies with  $A > 0.35$  are classified as mergers, while those which lie above the top line are early-types. Galaxies to the left of the middle line in Figure 20 & 21, are labelled mid-types and those to the right of this line are classified as late-types.

These criteria for identifying mergers and late-types appear more appropriate for our sample in the  $i_{775}$  and  $z_{850}$  bands, while galaxies are more mixed in these regions in stellar mass, having many more galaxies with high asymme-

tries, and spirals are not easily distinguished from merging systems. However, the uniqueness of the early-type region is more obvious in stellar mass maps, with most E galaxies in the  $i_{775}$  and  $z_{850}$  band plots falling into the mid-type region (Fig. 21).

We find that for our sample,  $z_{850}$  is the best band in which to measure these parameters for separating morphological types from each other. It can also be seen in Fig. 20 that the  $A$ - $C$  relation breaks down when viewed in bluer bands, as also shown for nearby galaxies in Taylor-Mager et al. (2007). We find that the scatter in  $A$ - $C$  increases for all galaxy types towards bluer wavelengths, the effect is more pronounced for late-type morphologies.

Figure 21 shows the  $A$ - $C$  relation for the stellar mass maps. There is a greater range in asymmetry values in stellar mass and the criterion suggested by Conselice (2003) for merging systems, of  $A > 0.35$ , even includes a few E and some eS galaxies. There is, however, still a clear separation in types between early and peculiar type systems, but the

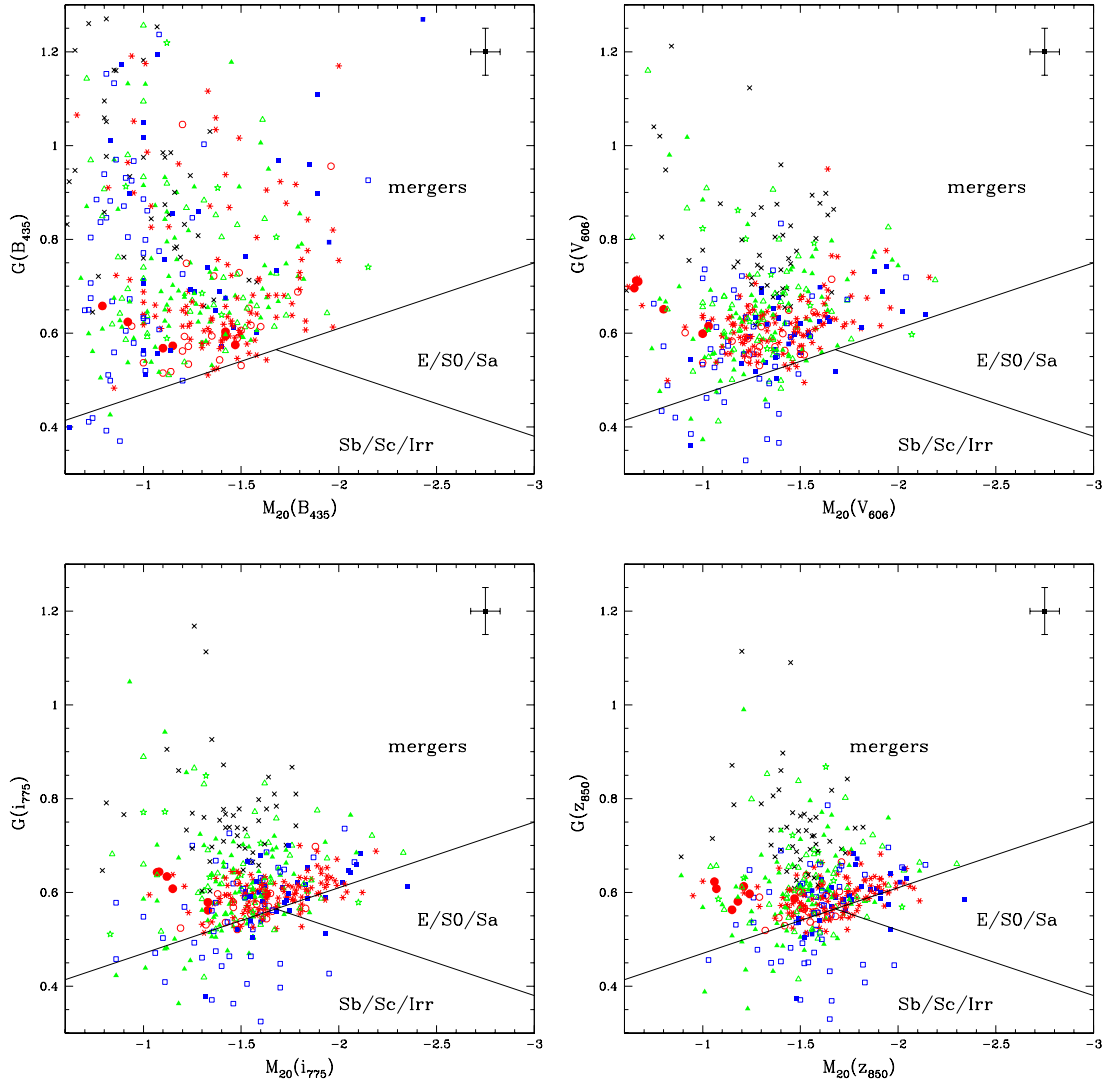


**Figure 22.** Gini- $M_{20}$  for the  $B_{435}$ ,  $V_{606}$ ,  $i_{775}$  and  $z_{850}$  bands. The solid lines mark the classification criteria of Lotz et al. (2004; Equations 10 and 11).

spirals (especially IS galaxies) significantly overlap between the two. This makes it difficult to distinguish between morphological types in stellar mass within  $A-C$ . However, given the fact that many of these spirals appear to have some kind of merger or formation mode, the stellar mass structure is superior for finding galaxies in active evolution.

#### 4.4.2 Gini vs. $M_{20}$

We plot the relation between  $G$  and  $M_{20}$  for light and stellar mass in Figures 22 and 23. The solid lines in Fig 22 are taken from Lotz et al. (2008), who used these parameters to classify their sample of normal galaxies and ULIRGs. Equation 10 describes the line above which Lotz et al. classify their sample as mergers, and Eq. 11 describes the line separating early and late-type galaxies.

$$G = -0.14 \cdot M_{20} + 0.33 \quad (10)$$

$$G = 0.14 \cdot M_{20} + 0.80 \quad (11)$$

We again see that the cleanest, in terms of separating morphological types, optical relation is in  $z_{850}$ , although our sample is not best represented by the Lotz et al. classifications in Gini- $M_{20}$  space, with many early-type galaxies falling into the merging region of the plot. This is partially due to the fact that  $G$  and  $M_{20}$  are calculated differently here then in Lotz et al., as described in §3.3 and Lisker et al. (2008). However, we cannot rule out that the classifications for this sample may be intrinsically different, and it is worrying that all of the edge-on galaxies fall into the merging region of  $G$ - $M_{20}$ . We also use a similar procedure to look at the same rest-frame wavelength as Lotz et al. does.

We modify the Lotz et al. (2008) relations for  $z_{850}$  (top) and stellar mass (bottom) and show this in Fig. 23. The solid lines in the  $z_{850}$  plot are our revisions to the Lotz et al. relations, based on our sample (Equations 12 for mergers and 13 for normal systems),

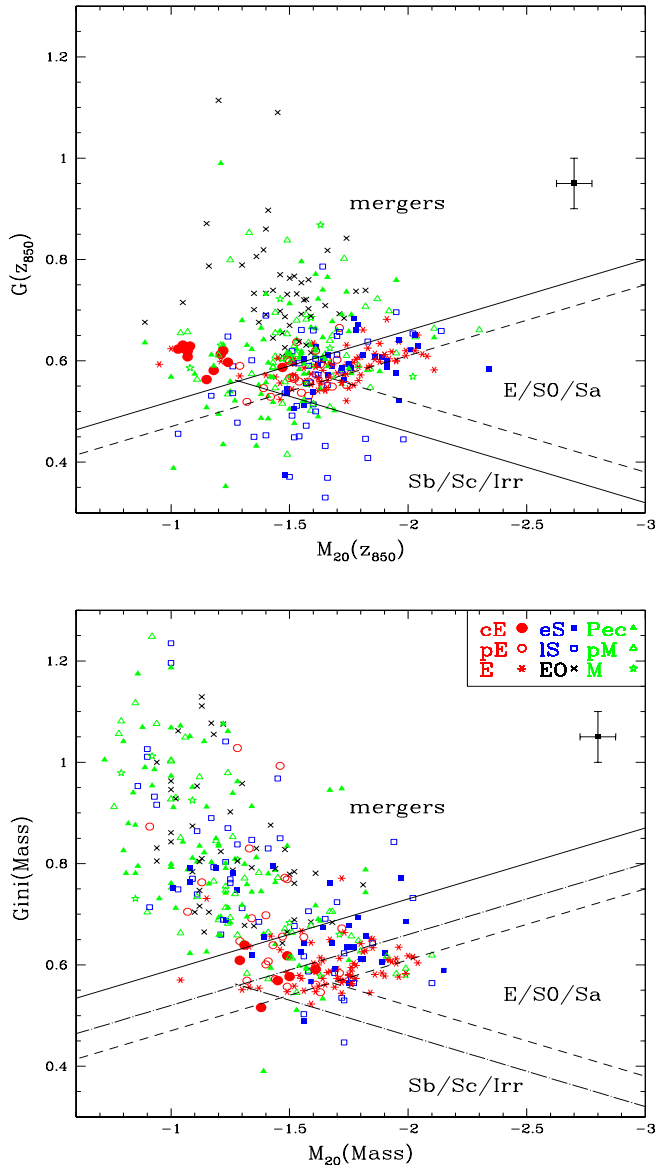


**Figure 23.** Gini- $M_{20}$  for  $z_{850}$  (top) and the stellar mass maps (bottom). In  $z_{850}$  (top) the dashed lines are the classification criteria of Lotz et al. (2004; Equations 10 and 11) while the solid lines mark our revised criteria in  $z_{850}$  (Equations 12 and 13). In stellar mass (bottom) the Lotz et al. criteria are marked by the dashed lines, our  $z_{850}$  criteria are shown by the dot-dashed lines and the solid line shows our separation of early and late types/mergers, in stellar mass.

$$G(z_{850}) = -0.14 \cdot M_{20}(z_{850}) + 0.38 \quad (12)$$

$$G(z_{850}) = 0.14 \cdot M_{20}(z_{850}) + 0.74 \quad (13)$$

while the dashed lines are the original Lotz et al. relations. In the bottom panel of Fig. 23, the solid line shows our revision of the merger defining line for the stellar mass maps, (Eq. 14),

$$G(M_{*}) = -0.14 \cdot M_{20}(M_{*}) + 0.45, \quad (14)$$

while here our relations for  $z_{850}$  and those of Lotz et al. are shown as dot-dashed and dashed, respectively.

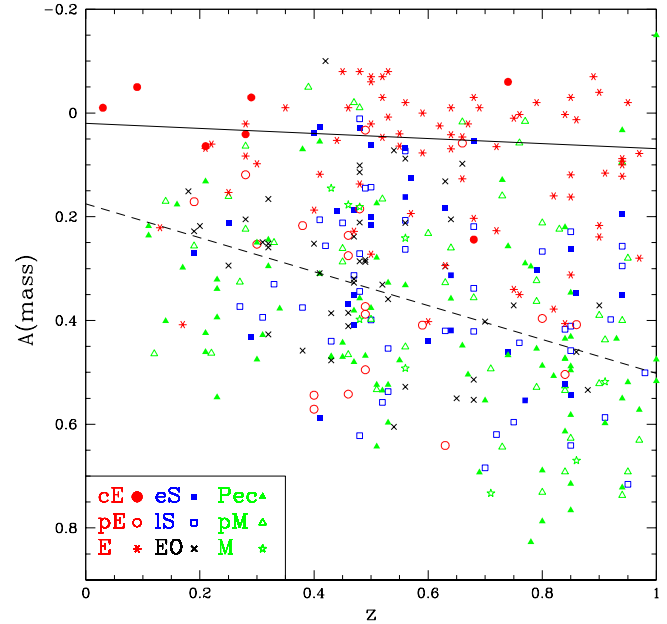


**Figure 24.** Asymmetry in stellar mass maps vs. redshift. The solid line shows the fit to the E galaxies (Eq. 15), which is approximately constant across redshifts ( $z$ ). The dashed line illustrates the fit to the late-type spiral galaxies (Eq. 16). The late-type spiral galaxies show a larger  $A(M_{*})$  with increasingly higher redshifts.

As with the relation for  $A(M_{*})-C(M_{*})$ , the  $G(M_{*})-M_{20}(M_{*})$  relation shows the same general trend as its  $z_{850}$  counterpart, but with a larger spread in values. The spirals, again, are not as neatly defined as in  $z_{850}$ , with the eS galaxies separated from the early-types and the late-type spirals and edge-on disk galaxies occupying the merging region. However, there is a clear separation in the stellar mass Gini vs.  $M_{20}$  which does not exist for the optical light. Several of the pE galaxies lie in the merger region, even as defined by the higher stellar mass line (Eq. 14). This has also been noted by Conselice et al. (2007), and is likely due to these objects having multiple nuclei.

The  $G(M_{*})-M_{20}(M_{*})$  relation shows a clear early/late-type split, defined by Eq. 14, as the Sb/Sc/Irr region, as described by Lotz et al. is not appropriate to apply to our sample in stellar mass. We discuss other correlations: asymmetry vs. clumpiness, concentration vs.  $M_{20}$ , size vs. concentration, and asymmetry vs.  $M_{20}$  in the appendix A. We evaluate in this appendix other scaling relationships between these non-parametric relationships, including asymmetry-clumpiness, concentration and  $M_{20}$ , size and concentration, and asymmetry and  $M_{20}$ .

#### 4.5 The Evolution of Galaxy Stellar Mass Structure with Redshift

In this section we investigate the changes in our galaxy stellar mass maps with redshifts. We take a quantitative approach here and find that at  $z < 1$  there is little change in the stellar mass structure with redshift, with the excep-

tion of the asymmetries of these galaxies which decreases for some galaxy types at  $z < 1$ .

We plot  $A(M_*)$  against redshift (Figure 24) where we can see a general trend for galaxies to become more asymmetric in stellar mass at higher redshifts. We find that not all galaxy types follow this pattern however, with the most notable exception being the ellipticals. As shown in Fig. 24 there is no trend for the ellipticals to become more asymmetric in stellar mass at higher redshifts.

We note that while the Es remain at approximately the same low asymmetries across the range in redshift, there is a trend for spiral galaxies to become increasingly asymmetric at higher redshifts. We measure this trend by fitting both the ellipticals (solid line) and IS (dashed line) galaxies, plotted in Figure 24 and quantified in Equations 15 and 16, below.

$$A_E(M_*) = 0.049(\pm 0.079) \cdot z + 0.021(\pm 0.056) \quad (15)$$

is the best fit for the ellipticals and for the late-type spirals, the best fit is,

$$A_{IS}(M_*) = 0.327(\pm 0.093) \cdot z + 0.175(\pm 0.064). \quad (16)$$

Equation 15 shows that the early-type galaxies retain approximately constant asymmetries across  $0 < z < 1$ . Equation 16 indicates that there is a relation for late-type spirals, such that  $A(M_*)$  increases with redshift.

We have already discussed in §4.3.3 how the late-type spiral galaxies have stellar mass asymmetries larger than their asymmetries in optical light. Since the late-type spirals are galaxies which have arms/disks that are larger/brighter than the bulge component, these galaxies are therefore dominated in terms of their light by their spiral structures and arms. These galaxies show the most diversity and contrast between spatial distributions within their M/L and stellar mass maps (e.g., Fig. 6).

We note that not all of the late-type spirals have high asymmetries in the stellar mass maps, some are as asymmetric or less than in the  $z_{850}$ -band (Fig. 16). Furthermore, we find that in general the disk galaxies with higher stellar mass map asymmetries have a bluer colour, which is the case at both high and low redshifts. In many of these cases, the structures are lopsided and/or contain outer features that remain after normalising by the M/L map. This interpretation of stellar mass being more localised than the light is consistent with a higher Gini index in the stellar mass bands than in the light.

Some of these asymmetric spirals, as well as many of the peculiars resemble the so-called ‘‘clump clusters’’ and clumpy spirals found by Elmegreen et al. (2005, 2007), especially in stellar mass maps. Their low concentration in mass is also similar to the Luminous Diffuse Objects (LDOs) found at similar redshifts (Conselice et al. 2004). Indeed, there are some late-type spirals galaxies that we would have classified differently, perhaps as Pec or pM systems, had we performed the classification in stellar mass, rather than in  $z_{850}$ . The clumps in galaxies found by Elmegreen et al. are also massive, with typical values in the region  $\sim 10^8 - 10^9 M_\odot$  (Elmegreen & Elmegreen 2005), and reside in young disks at high redshift. It is likely that some of our highly asymmetric late-type spiral galaxies are similar, or in the same class as these clumpy spirals. These features may also be the result of minor merger events.

## 5 CONCLUSIONS

We conduct a pixel by pixel study of the structures of 560 galaxies found in the GOODS-N field at  $z < 1$  within stellar mass maps and Hubble Space Telescope ACS *BViz* wavebands. We measure stellar masses for each pixel of each galaxy image from our *BViz* images by fitting to stellar population models. We use these values to construct stellar mass maps for our sample and compare morphologies in *BViz* and stellar mass. Our major findings and results include:

I. We construct stellar mass maps and mass-to-light ratio maps for each galaxy and we present examples of each morphological type, in the  $z_{850}$  band, stellar mass maps, and  $(M/L)_B$  in Figures 2 to 10. We find that some compact elliptical (cE) galaxies have blue cores, and more complicated internal structures than in either  $z_{850}$  or stellar mass would reveal on their own. Many of the peculiar ellipticals (pE) also have blue cores and we assert that these objects may have merged in their recent histories. The early and late-type spirals display more varied patterns. We find that for some of these galaxies, structures seen in light (e.g. spiral arms) are smoothed out in stellar mass. However, this effect does not hold true for all galaxies, nor for all features seen in light. Stellar mass and  $(M/L)$  maps of the ‘peculiar’ galaxies are complicated and vary across the sample. Although it is more difficult to make out features in stellar mass for galaxies that have very blue colours, structures not seen in light are revealed.

II. We compare the half-light radius,  $R_e$ , in  $z_{850}$  with half-mass radii for our sample as a function of morphological type. We find no systematic tendency for any particular morphological type to have larger  $R_e$  in stellar mass than in the  $z_{850}$  band, and thus conclude that there is no bias introduced by measuring galaxy sizes in  $z_{850}$ .

III. We find a clear tendency for many galaxies to be more asymmetric in stellar mass than in  $z_{850}$ . We also find that morphology correlates with asymmetries, with early-types having low  $A(M_*)$ , and late-types higher values of  $A(M_*)$ . We find a relation between colour and  $A(M_*)$  such that bluer galaxies have higher stellar mass asymmetry differences between optical light and stellar mass maps. The late-type spiral galaxies in the sample have higher  $A(M_*)$  than would be expected from their asymmetries in  $z_{850}$ . We discuss possible causes of this effect, including regions of enhanced star formation also possessing higher stellar masses, and the evolution of spirals. We note that these highly asymmetric spirals resemble the clumpy disks of Elmegreen et al. (2007), and Conselice et al. (2004) and are experiencing either minor merging activity, or bulge formation through accretion of disk material.

IV. We find that the Gini index in stellar mass is higher than in the  $z$ -band ( $G(M_*) > G(z_{850})$ ) for all galaxies except the early-types, indicating that most of the stellar mass in later morphological types is contained within fewer pixels. Late-type and peculiar morphologies show a trend for  $M_{20}(M_*) > M_{20}(z_{850})$ , suggesting that the brightest 20 percent of the brightest pixels is not necessarily where the greatest 20 percent of the stellar mass is located.

V. We investigate the relations between several combinations of the *CAS* parameters in *BViz* and stellar mass, and compare our results to previous morphological stud-

ies of this type (e.g. Conselice, Rajgor & Myers 2008; Lotz et al. 2004; 2008). We find that  $z_{850}$  is the most appropriate photometric band to utilise for a  $z < 1$  sample of galaxies with all morphologies, although stellar mass maps are better at distinguishing active galaxies from passive ones and is more a physical measure of structure.

We furthermore compare our sample classifications in  $G$ - $M_{20}$  to those of Lotz et al. (2008) and find that the Lotz et al. criteria do not best describe our sample. We revise the Lotz et al. (2008) criteria to best fit our sample in the  $z_{850}$ -band and within the stellar mass maps, and find that early-types, late-types and mergers can be separated. However, the edge-on disk galaxies remain problematic and cannot be distinguished from mergers in  $G(z_{850})$ - $M_{20}(z_{850})$ . We find that  $G(M_*)$ - $M_{20}(M_*)$  can be used to broadly separate early from late-type galaxies, but the criteria cannot distinguish between late-type/edge-on disks from peculiar/merger systems.

VI. We find a relationship between  $R_e$  and  $C$  (see appendix A) for early-type galaxies in both  $z_{850}$  and stellar mass. In each case we find that galaxies with higher concentrations have larger radii, and this relation is steeper in  $z_{850}$  than stellar mass. We also investigate asymmetry versus  $M_{20}$  and find that these parameters display a similar relation to  $A - C$  in  $i_{775}$  and  $z_{850}$ . In stellar mass,  $A(M_*)$ - $M_{20}(M_*)$  shows a tighter relation than  $A(M_*) - C(M_*)$ , with a clear separation between early and late-type systems. Thus, we conclude that, for all parameters, late-type spiral galaxies overlap with Pec/pM/M systems which may be ultimately taken from the same subset of galaxies. Structural studies in stellar mass do however track both minor and major merging events, and can be used to find galaxies in active galaxy evolution modes.

We thank the GOODS team for making their data public, and STFC for a studentship towards supporting this work and the Leverhulme Trust for support.

## REFERENCES

- Abraham, R.G., et al. 1996, MNRAS, 279, 47  
 Abraham, R.G., et al. 1999, MNRAS, 303, 641  
 Abraham, R.G., van den Bergh, S., Nair, P. 2003, AJ, 588, 218  
 Beauvais, C., Bothun, G. 1999, ApJS, 125, 99  
 Bershady, M.A., Jangren, J.A., & Conselice, C.J. 2000, AJ, 119, 2645  
 Bertone, S., Conselice, C.J. 2009, MNRAS, 396, 2345  
 Blanton, M.R. & Roweis, S. 2007, AJ, 133, 734  
 Bothun, G.D., 1986, AJ, 91, 507  
 Bruzual, G. & Charlot, S. 2003, MNRAS, 344, 1000  
 Buitrago, F., Trujillo, I., Conselice, C.J., Bouwens, R.J., Dickinson, M., Yan, H. 2008, ApJ, 687, 61L  
 Cassata, P., et al. 2010, ApJ, 714L, 79  
 Carrasco, E.R., Conselice, C.J., Trujillo, I. 2010, MNRAS, 405, 2253  
 Chabrier, G. 2003, ApJ, 586, 133L  
 Conselice, C.J., 1997, PASP, 109, 1251  
 Conselice, C.J., Bershady, M.A., & Jangren, A. 2000, ApJ, 529, 886  
 Conselice, C.J., Gallagher, J.S., Wyse, R.F.G. 2002, AJ, 123, 2246  
 Conselice, C.J. 2003, ApJS, 147, 1  
 Conselice, C.J. et al., 2003, AJ, 126, 1183  
 Conselice, C.J., et al. 2004, ApJ, 600, 139L  
 Conselice, C.J., Blackburn, J. A., Papovich, C., 2005, ApJ, 620, 564  
 Conselice, C.J. 2006a, ApJ, 638, 686  
 Conselice, C.J. 2006b, MNRAS, 373, 1389  
 Conselice, C.J., et al. 2007, MNRAS, 381, 962  
 Conselice, C.J., Rajgor, S. & Myers, R. 2008, MNRAS, 386, 909 (Paper I)  
 Conselice, C.J., Yang, C., Bluck, A.F.L. 2009, MNRAS, 394, 1956 (Paper III)  
 Conselice, C.J., Arnold, J. 2009, MNRAS, 397, 208  
 Elmegreen, D.M., Elmegreen, B.G., Rubin, D.S., Schaffer, M.A. 2005, ApJ, 631, 85  
 Elmegreen, D.M., Elmegreen, B.G., Ravindranath, S., Coe, D.A. 2007, ApJ, 658, 763  
 Ferguson, H.C., et al. 2004, ApJ, 600, 107L  
 Giavalisco, M., et al. 2004, ApJ, 600, 103L  
 Graham, A.W., Driver, S.P., Petrosian, V., Conselice, C.J., Bershady, M.A., Crawford, S.M., Goto, T. 2005, AJ, 130, 1535  
 Hernandez-Toledo, H.M., Avila-Reese, V., Conselice, C.J., Puerari, I. 2005, 129, 682  
 Lanyon-Foster, M.M., Conselice, C.J. & Merrifield, M.R. 2007, MNRAS, 380, 571  
 Lisker, T. 2009, ApJS, 179, 319  
 Lotz, J., Primack, J., Madau, P. 2004, AJ, 128, 163  
 Lotz, J.M., et al. 2008, ApJ, 672, 177  
 Maraston, C. 2005, MNRAS, 362, 799  
 Mobasher, B., et al. 2004, ApJ, 600, 167L  
 Oke, J.B. & Sandage, A. 1968, ApJ, 154, 21  
 Petrosian, V. 1976, ApJ, 209, 1L  
 Riciardelli, E., Trujillo, I., Buitrago, F., Conselice, C.J., 2010, MNRAS, 406, 230  
 Simard, L., et al. 2002, ApJS, 142, 1  
 Stanford, S.A., et al. 2004, AJ, 127, 131  
 Strauss, M.A., et al. 2002, AJ, 124, 1810  
 Taylor-Mager, V.A., Conselice, C.J., Windhorst, R.A., Jansen, R.A. 2007, ApJ, 659, 162  
 Trujillo, I., Conselice, C.J., Bundy, K., Cooper, M.C., Eisenhardt, P., Ellis, R.S. 2007, MNRAS, 382, 109  
 Weinzirl, T., et al. 2011, ApJ, 743, 87  
 Welikala, N., et al. 2011, arXiv: 1112.2657  
 Welikala, N., Connolly, A.J., Hopkins, A.M., Scranton, R., Conti, A. 2008, ApJ, 677, 970  
 Windhorst, R., et al. 2002, ApJS, 143, 113  
 Wirth, G.D., et al. 2004, AJ, 127, 3121

## APPENDIX A: APPENDICES

### APPENDIX B: STRUCTURE SCALING RELATIONS

In this appendix we describe several additional scaling relationships between structural and morphological parameters, not discussed in the body of the paper, for our galaxy sample. Many of the relations we see here confirm the conclusions we reached earlier. Furthermore, we list these for a complete overview of how structure correlates in the Hubble

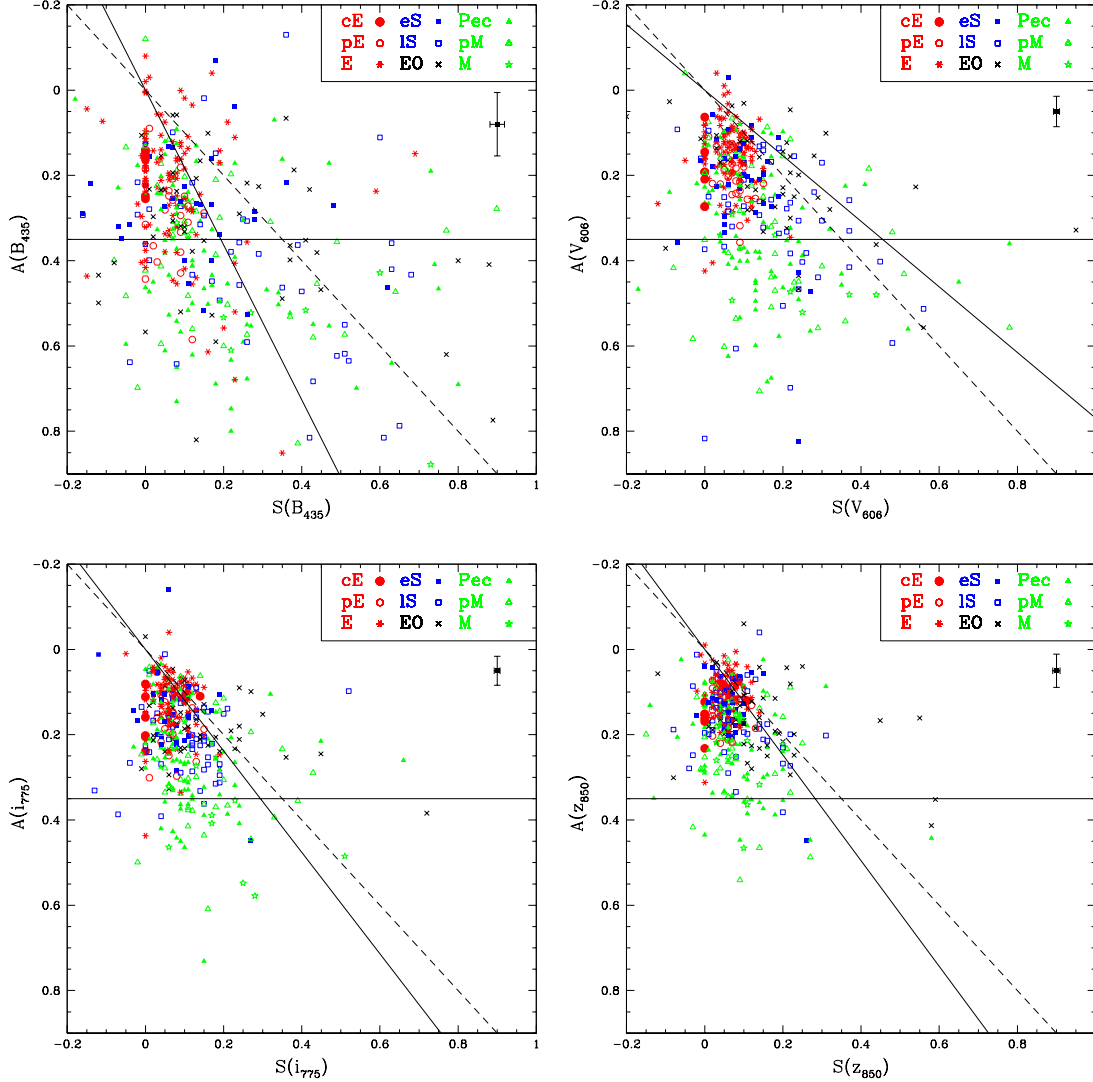


**Figure B1.** Asymmetry vs. clumpiness for the  $B_{435}$ ,  $V_{606}$ ,  $i_{775}$  and  $z_{850}$  bands. The solid horizontal line marks  $A = 0.35$ . The solid diagonal line shows the fit for each band to the elliptical and spiral (i.e., ‘normal’) galaxies in the sample and the dashed line marks the position of  $A = S$ . The black square point in the top right hand section of the plot illustrates the average error for the whole sample.

Space Telescope ACS  $BViz$  bands as well as in stellar mass maps.

### B1 Asymmetry vs. Clumpiness

We postulate that the many small scale asymmetries, measured by the clumpiness parameter, must approximate to the asymmetry of the galaxy as a whole. Figures B1 and B2 show the relation between  $A$  and  $S$  for  $B_{435}$ ,  $V_{606}$ ,  $i_{775}$ ,  $z_{850}$  and stellar mass, respectively. The horizontal solid line in each plot marks the  $A = 0.35$  position and the dashed line in each plot illustrates where  $A = S$ . The solid diagonal lines in each plot are the fits to the E, eS and IS galaxies in each band, which were forced to coincide at  $A = S = 0$ . These fits are shown below in Equations B1- B5, for each band respectively.

$$A(B_{435}) = 0.55(\pm 0.07) \cdot S(B_{435}) \quad (\text{B1})$$

$$A(V_{606}) = 1.30(\pm 0.08) \cdot S(V_{606}) \quad (\text{B2})$$

$$A(i_{775}) = 1.20(\pm 0.08) \cdot S(i_{775}) \quad (\text{B3})$$

$$A(z_{850}) = 1.24(\pm 0.08) \cdot S(z_{850}) \quad (\text{B4})$$

$$A(M_*) = 1.16(\pm 0.06) \cdot S(M_*) \quad (\text{B5})$$

It is evident that the relations are mostly steeper than  $A = S$ , although the fit in stellar mass comes closest to this equality. The  $A(M_*)$ - $S(M_*)$  relation thus is useful for identifying merger candidates. The criterion of  $A(M_*) > 0.35$  is too low for the stellar mass maps, instead we suggest that galaxies which lie in the region above  $A(M_*) > 0.6$  (horizontal dashed line, Fig. B2) and underneath the  $A(M_*)$ - $S(M_*)$  fit, be classified as mergers, and this could be adapted for use to calculate merger fractions across a range of redshifts.

The trend noted for the parameters to be less reliable in the bluer bands also holds here (Fig. B1). We note that the criteria  $A(z_{850}) > 0.35$  and  $A(z_{850}) > 1.24 \cdot S(z_{850})$  are ap-

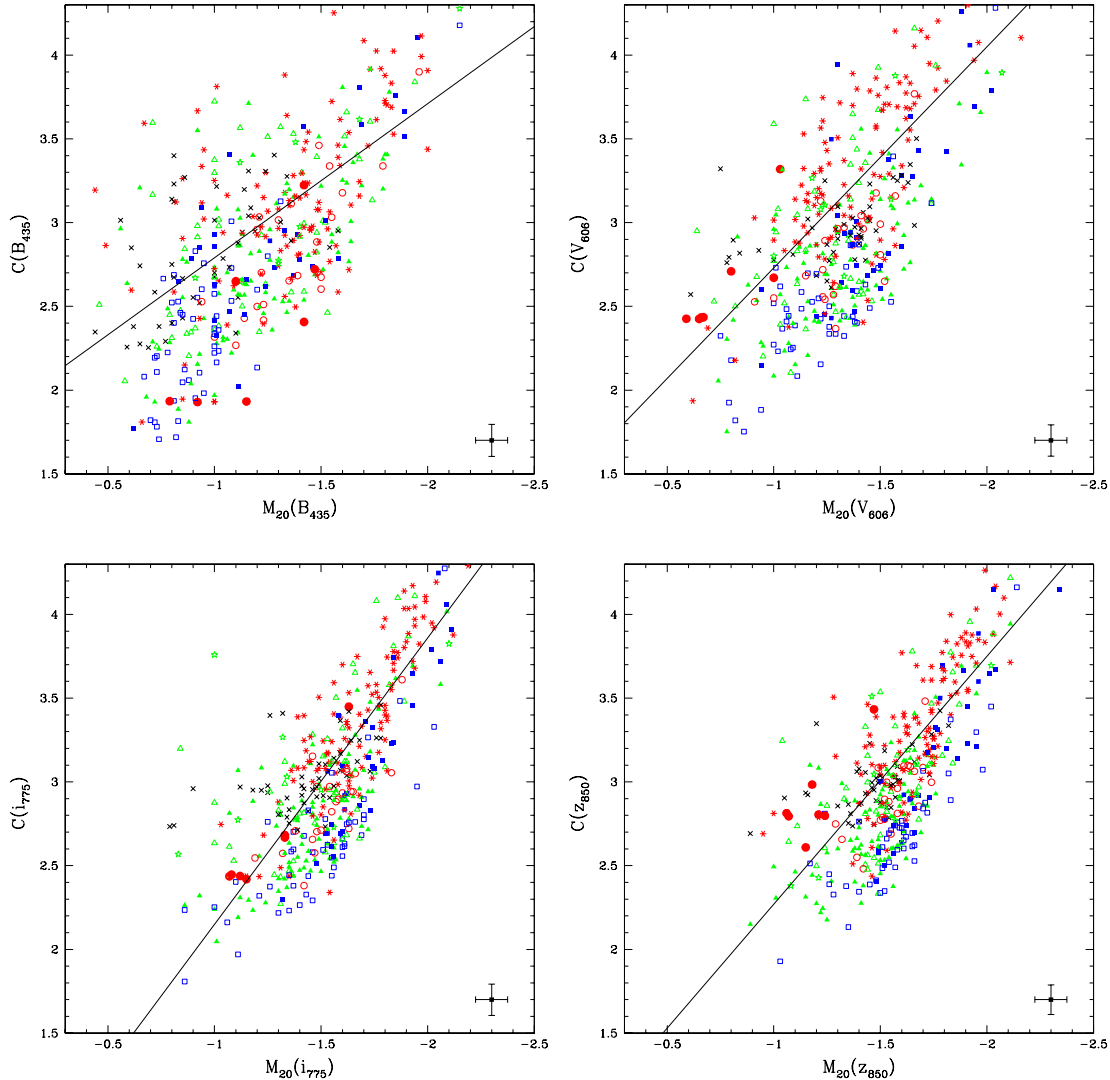


**Figure B3.** The relation between  $C$ - $M_{20}$  for the  $B_{435}$ ,  $V_{606}$ ,  $i_{775}$  and  $z_{850}$  bands. The solid lines show our fits to the E and eS galaxies in each band (Equations B6 to B9). The points are the same as in Figure A1.

appropriate for identifying merger candidates, and calculating merger fractions. The fits to  $A$ - $S$  for  $i_{775}$ ,  $z_{850}$  and stellar mass are very similar, despite the much larger scatter in  $A(M_*)$ .

## B2 $M_{20}$ vs. Concentration

In this section we investigate the relationship between  $M_{20}$  and  $C$  in  $B_{435}$ ,  $V_{606}$ ,  $i_{775}$ ,  $z_{850}$  and stellar mass (Figures B3 and B4). The solid lines in each plot show the fits to the E and eS galaxies in the sample. The forms of these fits are shown below in Equations B6 to B10.

$$C(B_{435}) = -0.92(\pm 0.12) \cdot M_{20}(B_{435}) + 1.87(\pm 0.16) \quad (\text{B6})$$

$$C(V_{606}) = -1.32(\pm 0.14) \cdot M_{20}(V_{606}) + 1.41(\pm 0.20) \quad (\text{B7})$$

$$C(i_{775}) = -1.71(\pm 0.13) \cdot M_{20}(i_{775}) + 0.44(\pm 0.22) \quad (\text{B8})$$

$$C(z_{850}) = -1.48(\pm 0.13) \cdot M_{20}(z_{850}) + 0.79(\pm 0.22) \quad (\text{B9})$$

$$C(M_*) = -1.42(\pm 0.08) \cdot M_{20}(M_*) + 0.81(\pm 0.13) \quad (\text{B10})$$

$M_{20}$  is anti-correlated with  $C$ , such that highly concentrated galaxies have lower  $M_{20}$  values. The general trend for concentration to increase as  $M_{20}$  decreases holds for all bands, although the scatter increases at higher values of  $M_{20}$  and lower  $C$ . The relation has a larger dispersion in the  $B_{435}$  and  $V_{606}$  bands, but this is more ordered than the random scatter seen in previous relations (Fig. B3, top panels). The relation is distinct in both  $i_{775}$  and  $z_{850}$ , with the early-type galaxies occupying the high  $C$ , low  $M_{20}$  region, the eS's having higher  $M_{20}$  values for their concentration and late-types generally having low  $C$  and high  $M_{20}$ .

This trend is also seen in the stellar mass maps (Fig. B4), but with greater separation between the morphological types than in  $i_{775}$  and  $z_{850}$ . The early-types also have high concentration and low  $M_{20}$ , although the spirals are more randomly distributed, and do not occupy any one region of the plot. The late/Pec/pM/M galaxies have higher  $M_{20}$

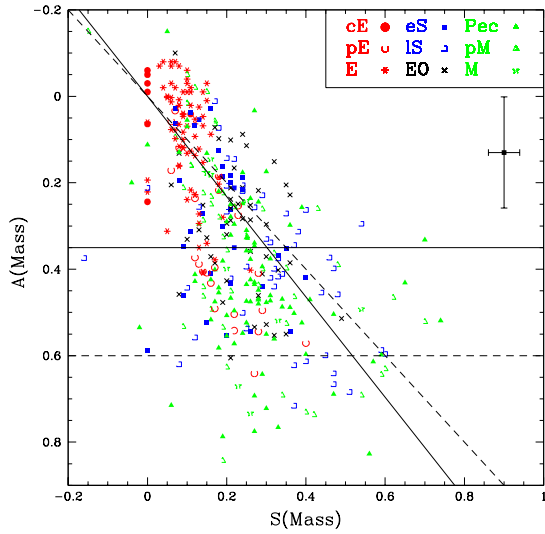


**Figure B2.** Asymmetry vs. clumpiness for the stellar mass maps. The convention is the same as in Fig. B1. The horizontal dashed line marks the position of  $A = 0.6$ , which we derive as a criterion for merger candidates in stellar mass.

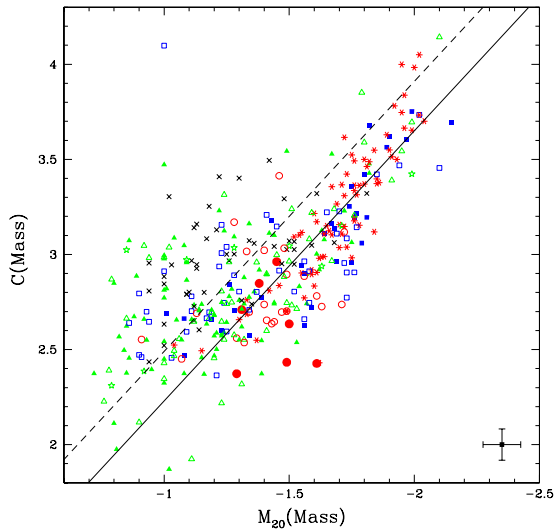


**Figure B4.** The relation between  $C$ - $M_{20}$  for the stellar mass maps. The solid line shows our fit to the E and eS galaxies in stellar mass (Eq. B10). The solid line is this relation plus  $2\sigma$ . The points are the same as in Figure A1.

values for their concentrations. The dashed line in Fig. B4 shows the fit plus  $2\sigma$  and we postulate that galaxies falling above this criterion can be picked out as merger candidates.

### B3 Size vs. Concentration

In this section we investigate the relation between galaxy size, as measured by the half-light radius,  $R_e$ , and concentration, in  $z_{850}$  and stellar mass. The top panel in Fig. B5 shows the relation in  $z_{850}$  and the bottom panel in stellar mass. We find that the early-types follow a linear relation-

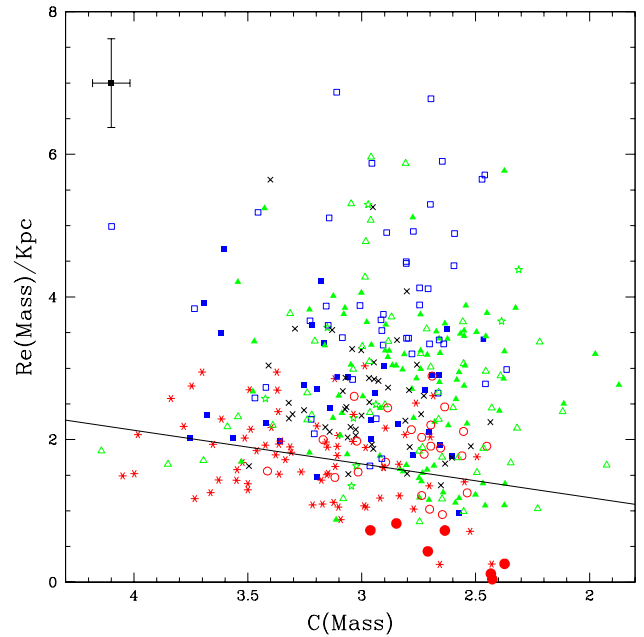
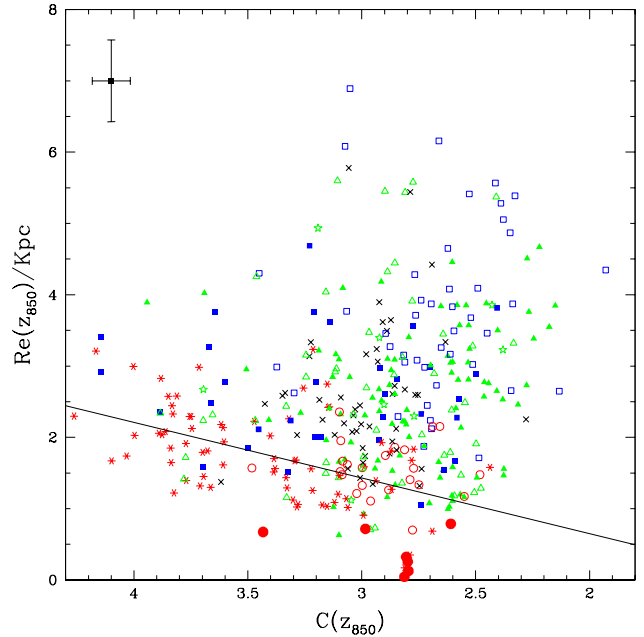


**Figure B5.** The relation between  $R_e$  and concentration for  $z_{850}$ -band images (top) and stellar mass maps (bottom). The solid lines show the fits to the E galaxies in each band (Equations B11 and B12). The points are the same as in Figure A1.

ship, and we have fit this relation for the E galaxies in  $z_{850}$  (Eq. B11) and stellar mass (Eq. B12).

$$Re(z_{850}) = 0.78(\pm 0.15) \cdot C(z_{850}) - 0.91(\pm 0.52) \quad (\text{B11})$$

$$Re(M_*) = 0.48(\pm 0.21) \cdot C(M_*) + 0.23(\pm 0.68) \quad (\text{B12})$$

The relation in  $z_{850}$  is steeper than in stellar mass, and both trends show that as  $R_e$  increases,  $C$  also increases. For normal galaxies,  $C$  is a tracer of stellar mass, such that lower  $C$  corresponds to less massive galaxies (Conselice 2003). In

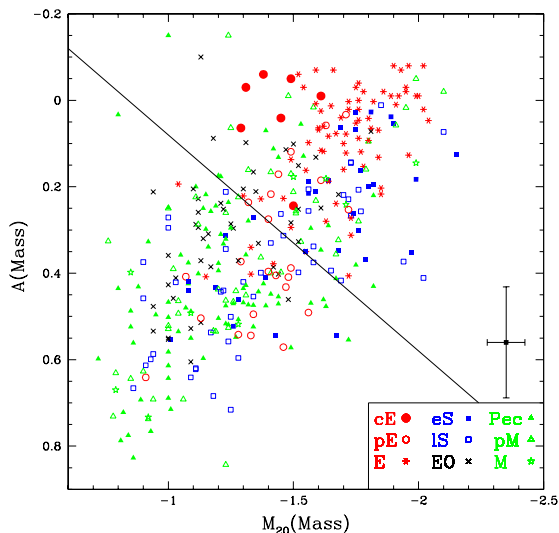


**Figure B7.** Asymmetry- $M_{20}$  for the stellar mass maps. The solid diagonal line marks our division between early and late-types/mergers.

both  $z_{850}$  and stellar mass we see that more concentrated galaxies have larger radii, and this effect is more pronounced in  $z_{850}$  than in stellar mass. No such relation is found for the late-types and Pec/pM/M systems.

Conselice & Arnold (2009) examine galaxies at  $z = 4-6$  in the Hubble Ultra Deep Field (HUDF) finding that early-types are smaller for their stellar mass at higher redshifts. They conclude that those galaxies that follow the  $C - R_e$  relation are in a relaxed state.

#### B4 Asymmetry vs. $M_{20}$

Here we investigate the relation between asymmetry and  $M_{20}$  in the  $B_{435}$ ,  $V_{606}$ ,  $i_{775}$ ,  $z_{850}$  bands (Fig. B6) and stellar mass (Fig. B7). As  $M_{20}$  is analogous to  $C$ , we would expect to see a similar relation between  $A - M_{20}$  and  $A - C$ . In Fig. B6 we see that in the  $BViZ$  bands we indeed find a similar relation in  $A - M_{20}$  to  $A - C$ , and could be used alongside  $A - C$  for classification purposes.

In stellar mass, however, the relation between  $A - M_{20}$  appears tighter than  $A(z_{850}) - C(z_{850})$ , such that galaxies with higher asymmetries have lower values of  $M_{20}$ . There is a clear separation between early and late-type galaxies in stellar mass, and we have included an approximate divide in this plot (solid line in Fig. B7), the form of which is shown below in Equation B13.

$$A(M_*) = -0.5 \cdot M_{20}(M_*) - 0.42 \quad (\text{B13})$$

Although this divide is very successful in separating early-types from Pec/pM/M systems, the spirals are spread over these two regions, again implying that measuring structural parameters in stellar mass does not distinguish between morphologies as well, although it traces physical processes better.

However, it is possible that viewing the stellar mass distribution of galaxies reveals different physical processes to those we expect to see in light. We have already discussed

the possibility that some highly asymmetric late-type spirals in our sample could be in the process of forming bulges. It is also possible that studies in stellar mass could provide clues as to the formation mechanism involved. The asymmetric late-type spirals, for example object 19535 (Figs. 6, 17), could be undergoing outside-in formation, perhaps through the accretion of smaller satellites. We could, therefore, be picking out systems experiencing minor merging events.

## APPENDIX C: CHARACTERISATION OF DIFFERENT GALAXY TYPES

At the start of this paper we describe how we classified each of our galaxies into one of nine type (§3.2). In this section, we described, based on our stellar mass map analysis, the properties of each of these galaxy types in terms of their optical and stellar mass structures, and what these imply about the evolution of different classes of galaxies.

While galaxy classification in terms of overall visual morphology is limited (Conselice 2006b), it is still useful for connecting galaxies at different redshifts, and for understanding how major nearby galaxy types such as disks and ellipticals are formed. Below we give details on the properties of each of the nine galaxy type that we have examined within GOODS.

### C1 Compact Es

Compact ellipticals are typically found in the late-type area of the C-A optical light diagram, but are within the early-type region of the C-A stellar mass diagram. The clumpiness values for these systems are also zero in all wavelengths and stellar mass due to the fact that these systems are so small this parameter cannot be reliably measured. The concentrations of these systems are always quite low, with  $C = 2.5-3$ , at the resolution limit where we can measure these values, suggesting that they are not similar to giant ellipticals (e.g., Conselice 2003).

Some interesting features appear when we compare the quantitative properties of cEs as measured in optical light to those in stellar mass maps. One of these is that for all cEs, the size measured in the stellar mass maps are always larger than for those measured in the reddest band,  $z_{850}$ . The asymmetry measured in stellar mass maps is also quite low, and lower than in the  $z_{850}$ , perhaps due to the fact that the asymmetric light is brought to a lower level within the stellar mass images compared to the optical light. The  $M_{20}$  parameter is also quite different between the stellar mass maps and the  $z_{850}$ , such that  $M_{20}$  is higher (less negative) in the  $z_{850}$ . This implies that the light distribution is more concentrated in the stellar mass maps, likely due to the blue coloured core.

### C2 Ellipticals

First, we find that just based on colours, there is a wide diversity at a given redshift (see Figs. 12 and 13) - an indication that at higher redshifts there is a range of elliptical galaxy star formation histories, something that has been recognised for some time (e.g., Stanford et al. 2004; Conselice et al. 2007). Simply based on the C-A diagram with

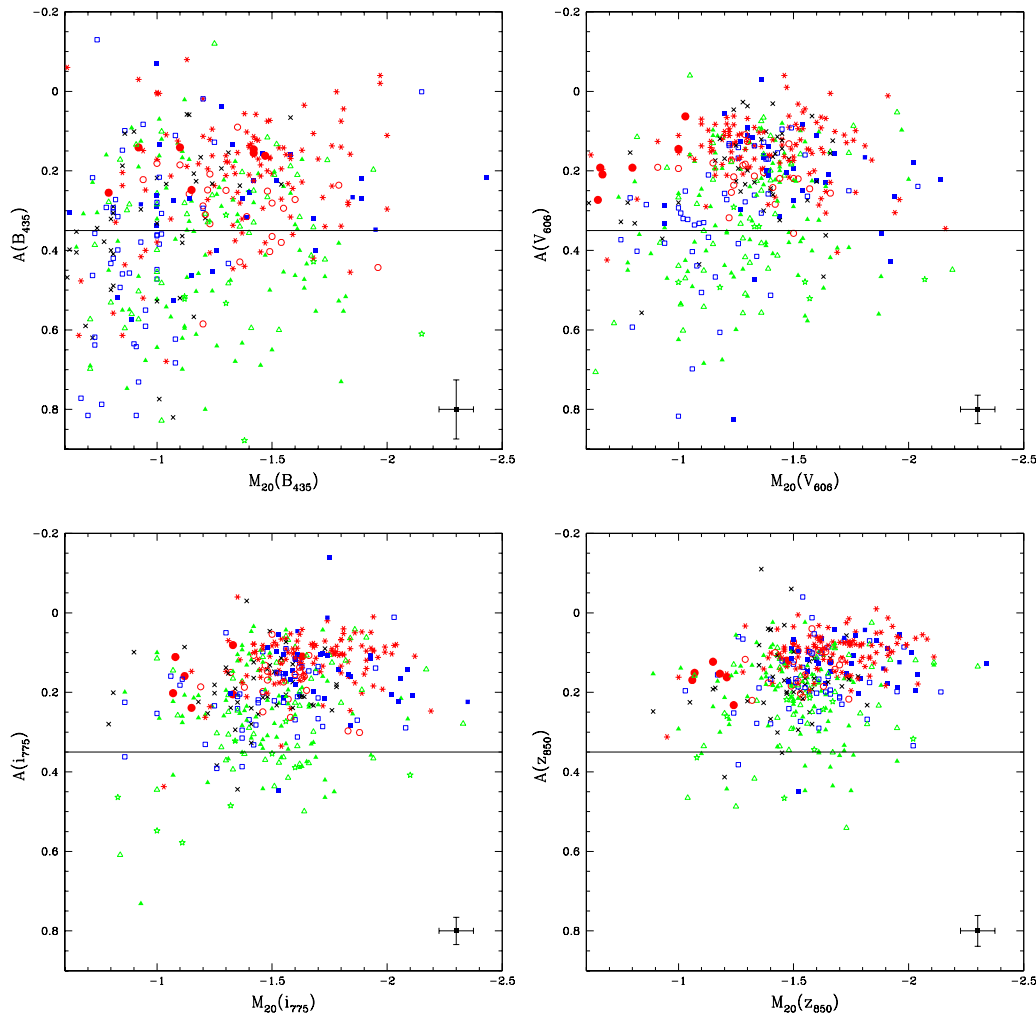


**Figure B6.** Asymmetry- $M_{20}$  for the  $B_{435}$ ,  $V_{606}$ ,  $i_{775}$  and  $z_{850}$  bands. The horizontal solid line marks  $A = 0.35$  in each band. The points are the same as in Fig. A1.

optical light (Fig. 20) it appears that most of the early-types are found in the region of C-A space classifiable as mid-types. This is commonly seen for high redshift ellipticals which appear more asymmetric than their  $z = 0$  counterparts (e.g., Conselice et al. 2007). Ellipticals do have generally lower Gini and  $M_{20}$  indices, however there is still some spread in their values.

The stellar mass maps reveal that ellipticals appear to become more ‘diffuse’ within stellar mass maps. However the sizes are either very similar in stellar mass maps or even slightly smaller, than in the corresponding  $z_{850}$ -band image. The Gini and the  $M_{20}$  parameters do not change significantly between the stellar mass maps and the  $z_{850}$ -band image. However, we find that some of the ellipticals are slightly more asymmetric in stellar mass maps than in the  $z$ -band, although many of these systems tend to be bluer galaxies. The ellipticals also tend to become less concentrated in stellar mass compared with the  $z_{850}$  band (Fig. 15).

Finally, the elliptical galaxies are one of the few types which do not change significantly in terms of their Gini and  $M_{20}$  values between stellar mass and the  $z_{850}$ , and this re-

sults in these systems having a well defined location in the stellar mass Gini/ $M_{20}$  diagram (Fig. 23).

### C3 Peculiar Ellipticals

The peculiar ellipticals are a galaxy type which has been recognised to exist up to at least  $z = 1.4$  before (e.g., Conselice et al. 2007). These peculiar ellipticals appear elliptical in overall morphology, but have internal structure suggesting that they have recently undergone some type of assembly. These galaxies are not uncommon, and are more often seen than the compact elliptical type.

These galaxies are more asymmetric and less concentrated than the Es - with all having concentrations,  $C < 3$ . They are quite distinct from the ellipticals in the CA plane and are bluer by  $\sim 0.5$  magnitudes from the giant ellipticals. These blue features can be readily seen within the M/L maps for these systems (Fig. 3). These galaxies often appear more elliptical in the stellar mass maps once their M/L variations have been taken into account.

Another difference between the pEs and the Es is that

these systems have half-light (or half-mass) radii which are nearly always bigger in the stellar mass maps than in the  $z_{850}$  band. This is a sign for star formation activity in the cores of these galaxies, since the bluer material in the core is less prominent in the stellar mass maps, giving them a larger effective radius. This can also be seen in the fact that the asymmetry in the stellar mass maps is generally higher than in the  $z_{850}$  band for these systems, which is another indication that they are undergoing some form of star formation.

The Gini values for these systems are higher in the stellar mass band than in  $z_{850}$ , which demonstrates that the stellar mass distribution is more concentrated in bright (but non-central) pixels than the light, as the light is less equally distributed than the stellar mass. The location of the pEs is similar to that of the Es in the Gini/ $M_{20}$  plane.

#### C4 Spirals

The spiral galaxies are amongst the most interesting for this study given that they often contain two major stellar population types segregated spatially. Traditionally this is seen as an older stellar population making up the bulge or centre, and the spiral arms consisting of younger stellar populations.

We find that the early-type spirals, those whose apparent bulge is brighter/larger than its apparent disk, are quite blue in colour. This difference is very obvious when examining the M/L ratio maps for these galaxies (Fig. 5), although the differences are not as obvious as with the late-type spirals. Nevertheless, these systems often appear to have a blue outer M/L ratio and a redder inner one, although there are examples where this is not the case.

The sizes of these galaxies does not change significantly between the stellar mass maps and the  $z_{850}$  band images. There are however some differences between the stellar mass maps and the  $z_{850}$  band images within the various parameters. The most significant of these is that the asymmetry parameter is higher in the stellar mass maps than in the  $z_{850}$  band imaging as discussed in detail in §4.3.3. The Gini parameter is also higher within the stellar mass maps than within the  $z_{850}$  by roughly 10 percent. This implies that the stellar mass is distributed in fewer pixels than in the light for spirals. The distribution of  $M_{20}$  values is similar between the light and stellar mass, suggesting that the spatial distribution is similar.

One notable feature of the spiral galaxies in general is that they have a much larger range of asymmetry values within the stellar mass images. In fact, their values are often as high as the peculiar galaxies, suggesting that within stellar mass maps these parameters cannot easily distinguish between mergers and spirals with mixed stellar populations.

#### C5 Peculiars/Mergers

The Peculiars, Pre-Mergers and Mergers all have similar patterns in the CAS space in both the stellar mass maps and within the  $z_{850}$  diagrams. These are the most asymmetric and bluest galaxies in our sample, and are likely in some phase of a merger, as has been described earlier in e.g., Conselice et al. (2003, 2008).

These peculiars (a term we use here for all three of these

types) do not change in size much between the stellar mass and the  $z_{850}$  image. However, the asymmetry in the stellar mass band is higher than for the  $z_{850}$  band. This is likely due to the stellar mass within these galaxies being more concentrated in fewer locations. The  $M_{20}$  also shows that the light is less concentrated in than the stellar mass, showing that the stellar mass is more distributed spatially than in light, suggestive of a merging systems. In fact, these peculiars have the highest asymmetries,  $M_{20}$ , and Gini indices.